

Large-scale Structures revealed by Wavelet Decomposition¹

Li-Zhi Fang² and Jesús Pando³

Department of Physics
University of Arizona
Tucson, AZ 85721, USA

arXiv:astro-ph/9701228v1 29 Jan 1997

¹The lecture of LZF at the 5th Current Topics of Astrofundamental Physics, Erice, Sicily, 7-15 September 1996

²Email address: fanglz@time.physics.arizona.edu

³jpando@soliton.physics.arizona.edu

Contents

1	Introduction	3
2	Discrete wavelet transform of density fields	5
2.1	An example: Haar wavelet	5
2.2	Multiresolution analysis	8
2.3	Compactly supported orthogonal bases	9
2.4	DWT decomposition	10
2.5	Relationship between Fourier and DWT expansion	13
2.6	Comparison with the Fourier transform	14
3	A DWT Estimation of the Probability Distribution Function	16
3.1	One-point distribution of FFCs	16
3.2	“Ensemble” of FFCs	17
3.3	Scale mixing	18
3.4	Spectrum of FFC cumulants	18
4	Local power spectrum	19
4.1	Power Spectrum with respect to DWT basis	19
4.2	Relationship between Fourier and DWT Spectra	20
4.3	Finite size and complex geometry of samples	21
5	Measures of non-Gaussianity	23
5.1	Spectra of skewness and kurtosis	23
5.2	Distribution of clumps	24
5.3	Suppression of shot noise	26
6	A preliminary result using DWT: Lyα forests	28
6.1	LSS Problems of Ly α clouds	28
6.2	Flatness of power spectrum	29
6.3	Kurtosis on large scales	31
6.4	Structures identified by multiresolution analysis	36
6.5	Discrimination among models	37
7	Miscellaneous topics	41
8	Outlook	45
A	Relationship between Fourier coefficients and FFCs	46
B	Parseval theorem of the DWT	47
C	References	49

1 Introduction

Large scale structure (LSS) study of Big Bang cosmology tries to explain how an initially flat or smooth 3-dimensional surface described by the Robertson-Walker metric evolved into a wrinkled one. In terms of density and velocity fields, it explains how an initially homogeneous and Hubble-expanding mass distribution evolved into its present inhomogeneous state. It is generally believed that LSS was initiated by fluctuations formed at the early universe, and that the subsequent clustering was brought about by gravitational interaction between baryonic and dark matter (Kolb & Turner 1989). As a result, like the physics of dynamical critical phenomena, turbulence, and multiparticle production in high energy collisions, problems in LSS are typical of structure formation due to stochastic forces and non-linear coupling (Berera & Fang 1994, Barbero et al 1996). The cosmic mass (or number) density distribution $\rho(x)$ can be mathematically treated as a homogeneous random field.

Traditionally, the statistics, kinetics and dynamics in LSS are represented by the Fourier expansion of the density field, $|\rho(k)|$. For instance, the behavior of the LSS in scale space can effectively be described by the power spectrum of perturbations $P(k) = |\rho(k)|^2$. In the case where the homogeneous random field $\rho(x)$ is Gaussian, all statistical features of $\rho(x)$ can be completely determined by the amplitude of the Fourier coefficients. In other words, the two-point correlation function, or its Fourier counterpart the power spectrum, are enough to describe the formation and evolution of the LSS.

However, the dynamics of LSS, such as clustering given by gravitational instability, is non-linear. Even if the field $\rho(x)$ is initially Gaussian, the evolved density field will be highly non-Gaussian. To describe the dynamics of the LSS knowledge of the phase of the Fourier coefficients $\rho(k)$ is essential. As is well known, it is difficult, even practically impossible, to find information about phase of the Fourier coefficients as soon as there is some computational noise (Farge 1992). This lack of information makes the description of LSS incomplete. Even in the case where the phases are detectable, the pictures in physical space, $\rho(x)$, and the Fourier space, $\rho(k)$ are separated. From the former we can only see the scales of the structures, but not the positions of the considered structures, and *vice versa* from the later. It has been felt for some time that the separate descriptions between Fourier (scale) and physical (position) spaces may lead to missing key physics.

In order to resolve this problem, methods of space-scale-decomposition (SSD) which might provide information about the phase (or position) and scale of the considered structures have been developed. The possibility of simultaneously localizing in both frequency (scale) and time (position) is not new in physics. Anybody who listens to music knows that they, at any time, can resolve the frequency spectrum. The problem of how to perform this time resolution is also not new in physics. Wigner functions in quantum mechanics, and the Gabor transform (Fourier transform on finite domain) were early approaches.

Speaking simply, SSD represents a density field as a superposition of density perturbations

localized in both physical and scale spaces. For instance, identification of clusters from a galaxy distribution by *eyes* is a SSD. Generally, all methods of identifying clusters and groups from surveys of galaxies or samples of N-body simulation are SSD. One can list several popular SSDs in cosmology as follows: smoothing by a window function, or filtering technique; percolation; the friend-to-friend algorithm; count in cells (CIC).

A common problem of most of the above mentioned SSDs is that the bases, or representations, given by these methods is incomplete. Unlike the Fourier representation $\rho(k)$, these SSDs lose information contained in the density field $\rho(r)$. For instance, one can completely reconstruct the density field $\rho(x)$ by the Fourier coefficients $\rho(k)$, but cannot do the same using window filters, CIC, percolation etc.

All these SSDs are, directly or indirectly, the precursors to the DWT (Discrete Wavelet Transform). The DWT is also a SSD, but is based on bases sets which are orthogonal and complete. The DWT is invertible and admissible making possible a complete representation of LSS without losing information. Unlike the Fourier bases (the trigonometric functions) which are inherently nonlocal, the DWT bases have limited spatial support. The DWT allows for an orthogonal and complete projection on modes localized in both physical and space spaces and makes possible a multiscale resolution.

Moreover, the orthogonal bases of the DWT are obtained by (space) translation and (scale) dilation of one scale function (Meyer 1992, 1993; Daubechies 1992). They are self-similar. This translation-dilation procedure allows for an optimal compromise: the wavelet transform gives very good spatial resolution on small scales, and very good scale resolution on large scales. Therefore, the DWT is able to resolve an arbitrary density field simultaneously in terms of its position variable and its conjugate counterpart in Fourier space (wavenumber or scale) up to the limit of uncertainty principle.

There have been attempts to use the continuous wavelet transform (CWT) to analyze LSS (Slezak, Bijaoui & Mars 1990; Escalera & Mazure 1992; Escalera, Slezak & Mazure 1992; Martinez, Paredes & Saar 1993). However, since 1992 it has become clear that the CWT is a *poor* or even *impossible* method to use as a reasonable SSD. The difference between CWT and DWT is mathematically essential, unlike the case for the Fourier transform, for which the continuous-discrete difference is only technical (Yamada & Ohkitani 1991; Farge 1992; Greiner, Lipa & Carruthers 1995).

These properties of the DWT make it unique among the various SSD methods. One can expect that some statistical and dynamical features of LSS can easily, and in fact *only*, be described by the DWT representation. The DWT study of LSS now is in a very preliminary stage. Nevertheless, results have shown that the DWT can reveal aspects of LSS behavior which have not been seen by traditional methods (Pando & Fang 1995, 1996a, 1996b; Huang et al 1996). These DWT-represented features have also been found to be effective for discriminating among models of LSS formation.

As we will show the DWT opens a new dimension in the study of the statistics and dynamics

of the LSS.

2 Discrete wavelet transform of density fields

The real difference in using the discrete wavelet transform (DWT) as compared with say, Fourier techniques, comes when one deals with samples of finite extent. Since both the bases are complete, the information revealed by both these techniques is equivalent when the function is continuous and the limits of the respective inner products or sums can be calculated at infinity. However, once the function is not continuous (or, rather, not continuously sampled) or the sum cannot be calculated to infinity, the two representations reveal different aspects of the distribution. But this is always the case when dealing with either observational data or simulated data. Limited resolution always forces one to sample a function at intervals, and no sum can be calculated to infinity. Unlike the Fourier transform, the difference between the continuous and discrete transform is not merely technical (Yamada & Ohkitani 1991; Farge 1992; Greiner, Lipa & Carruthers 1995). One does not merely replace the limit of a sum with infinity and then take a limit. By construction, the discrete and continuous wavelet transform are quite different.

2.1 An example: Haar wavelet

Let us first consider a 1-dimensional (1-D) density field $\rho(x)$ over a range $0 \leq x \leq L$. It is not difficult to extend the 1-D analysis to higher dimensions. It is convenient to use the density contrast defined by⁴

$$\epsilon(x) = \frac{\rho(x) - \bar{\rho}}{\bar{\rho}} \quad (2.1)$$

where $\bar{\rho}$ is the mean density in this field. Actually, observed data and simulated samples can only provide density distributions with finite resolution, say Δx . Hence, without loss of information, $\epsilon(x)$ can be expressed as a histogram with 2^J bins (Figure 1), where J is taken large enough so that $L/2^J < \Delta x$ i.e.

$$J \leq \text{mod}(|\ln \Delta x| / \ln 2) + 1, \quad (2.2)$$

The histogram is labeled so that the 2^J bins are designated by an integer, l , running from $0 \leq l \leq 2^J - 1$. Bin l covers a range from $Ll2^{-J}$ to $L(l+1)2^{-J}$. The samples can fully be described by the 2^J $\epsilon_{J,l}$ ($0 \leq l \leq 2^J - 1$) defined by

$$\epsilon_{J,l} = \epsilon(x), \quad Ll2^{-J} \leq x \leq L(l+1)2^{-J}. \quad (2.3)$$

Using $\epsilon_{J,l}$, we can rewrite $\epsilon(x)$ as

$$\epsilon(x) = \epsilon^J(x) \equiv \sum_{l=0}^{2^J-1} \epsilon_{J,l} \phi_{J,l}^H(x) \quad (2.4)$$

⁴We do not as usual denote the density contrast by δ , because of possible confusion with the Kronecker δ symbol

where the $\phi_{J,l}^H(x)$ are given by

$$\phi_{J,l}^H(x) = \begin{cases} 1 & \text{for } Ll2^{-J} \leq x \leq L(l+1)2^{-J} \\ 0 & \text{otherwise.} \end{cases} \quad (2.5)$$

Actually, $\phi_{J,l}^H(x)$ is a top-hat window function on resolution scale $L/2^J$ and at position $Ll2^{-J} \leq x \leq L(l+1)2^{-J}$.

Expression (2.5) can be generalized to top-hat window functions on different scales. We first define a top-hat scaling function as

$$\phi^H(\eta) = \begin{cases} 1 & \text{for } 0 \leq \eta \leq 1 \\ 0 & \text{otherwise.} \end{cases} \quad (2.6)$$

Thus, one can construct a set of top-hat window functions by a translation and dilation of the scaling function (2.6) as ⁵

$$\phi_{j,l}^H(x) = \phi^H(2^j x/L - l), \quad (2.7)$$

where j, l are integers, and $j \geq 0, 0 \leq l \leq 2^j - 1$. Obviously, $\phi_{j,l}^H(x)$ is a normalized top-hat window function on scale $L/2^j$ and at the position $Ll2^{-j} \leq x \leq L(l+1)2^{-j}$. $\phi_{j,l}^H(x)$ is called the mother function.

If we smooth the density contrast $\epsilon(x)$ by the mother function $\phi_{j,l}^H(x)$ on scale $j = J - 1$, we have an approximate expression of $\epsilon(x)$ as

$$\epsilon^{J-1}(x) = \sum_{l=0}^{2^{J-1}-1} \epsilon_{J-1,l} \phi_{J-1,l}^H(x) \quad (2.8)$$

where the mother function coefficients (MFCs) $\epsilon_{J-1,l}$ are given by

$$\epsilon_{J-1,l} = \frac{1}{2}(\epsilon_{J,2l} + \epsilon_{J,2l+1}). \quad (2.9)$$

Similarly, we can continue this procedure to find smoothed distributions $\epsilon^j(x)$ on scales $j = J - 2, J - 3, \dots$ as

$$\epsilon^j(x) = \sum_{l=0}^{2^{j-1}-1} \epsilon_{j,l} \phi_{j,l}^H(x) \quad (2.10)$$

where the j -th MFCs can be found from $(j+1)$ -th MFCs by

$$\epsilon_{j,l} = \frac{1}{2}(\epsilon_{j+1,2l} + \epsilon_{j+1,2l+1}). \quad (2.11)$$

These results are nothing new. In fact they are window smoothing on a scale-by-scale basis as shown in Figure 1. The $\epsilon_{j,l}$ contain less information than $\epsilon_{j+1,l}$. In order not to lose any information as a result of the smoothing, we should calculate the difference between the smoothed distributions on succeeding scales, say $\epsilon^{j+1}(x) - \epsilon^j(x)$. Figure 1 also plots these differences.

⁵Actually, eq.(2.7) is not a dilation of eq.(2.6), but a compression. We use the word "dilation", because in the wavelet literature the factor $1/2^{-j}$ is called the scale dilation parameter, regardless if it is larger than 1.

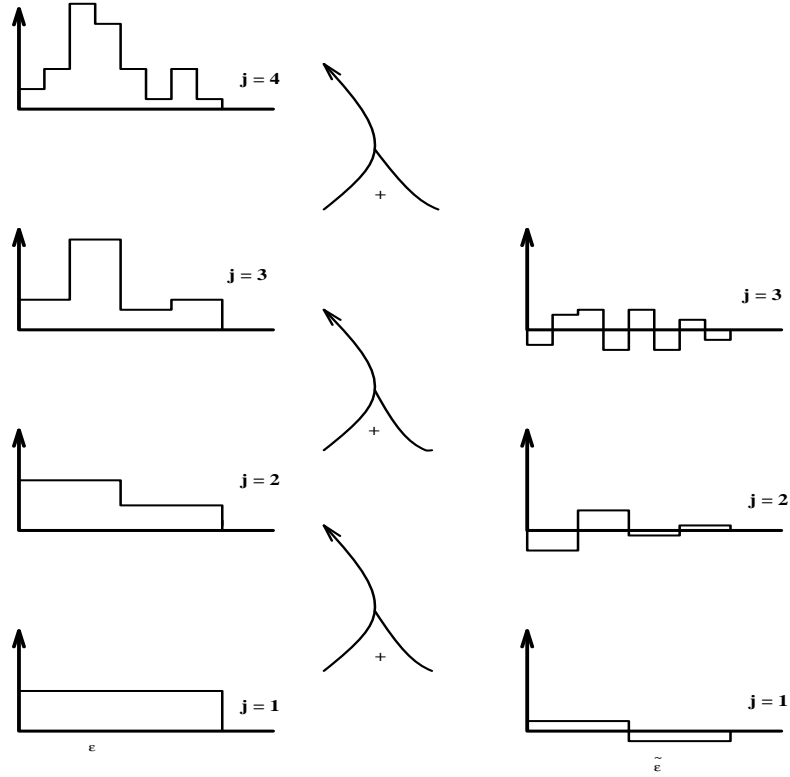


Figure 1: A Haar wavelet multiresolution decomposition. The original sample is shown by the top left figure. Its resolution is $j = 4$. The left column is the reconstructed distributions of the MFCs $\epsilon_{j,l}$ on scales $j = 3, 2, 1$. The right column of histograms show the distribution of FFCs, $\tilde{\epsilon}_{j,l}$ on the corresponding scale j .

To describe this difference, we define a wavelet as

$$\psi^H(\eta) = \begin{cases} 1 & \text{for } 0 \leq \eta \leq 1/2 \\ -1 & \text{for } 1/2 \leq \eta \leq 1 \\ 0 & \text{otherwise.} \end{cases} \quad (2.12)$$

This is the Haar wavelet, and it is the reason that we used a superscript H on the functions $\phi(x)$ and $\psi(x)$. As with the mother functions, one can construct a set of $\psi_{j,l}^H(x)$ by dilating and translating eq.(2.10) as

$$\begin{aligned} \psi_{j,l}^H(x) &= \psi^H(2^j x/L - l) \\ &= \begin{cases} 1 & \text{for } Ll2^{-j} \leq x \leq L(l + 1/2) 2^{-j} \\ -1 & \text{for } L(l + 1/2)2^{-j} \leq x \leq L(l + 1) 2^{-j} \\ 0 & \text{otherwise.} \end{cases} \end{aligned} \quad (2.13)$$

$\psi_{j,l}^H(x)$ is called the father function (Meyer 1993) ⁶

⁶In some of the literature $\psi_{j,l}^H(x)$ is called the mother function, while $\phi_{j,l}^H(x)$ the father function. This is unfortunate but we hope this confusion will not lead to too many misunderstandings.

From eqs.(2.7) and (2.13), we have

$$\begin{aligned}\phi_{j,2l}^H(x) &= \frac{1}{2}(\phi_{j-1,l}^H(x) + \psi_{j-1,l}^H(x)), \\ \phi_{j,2l+1}^H(x) &= \frac{1}{2}(\phi_{j-1,l}^H(x) - \psi_{j-1,l}^H(x)).\end{aligned}\tag{2.14}$$

Eq.(2.4) can be rewritten as

$$\begin{aligned}\epsilon^J(x) &= \sum_{l=0}^{2^{J-1}-1} \epsilon_{J-1,l} \phi_{J-1,l}^H(x) + \sum_{l=0}^{2^{J-1}-1} \tilde{\epsilon}_{J-1,l} \psi_{J-1,l}^H(x) \\ &= \epsilon^{J-1}(x) + \sum_{l=0}^{2^{J-1}-1} \tilde{\epsilon}_{J-1,l} \psi_{J-1,l}^H(x)\end{aligned}\tag{2.15}$$

where we used eqs.(2.8) and (2.9), and

$$\tilde{\epsilon}_{J-1,k} = \frac{1}{2}(\epsilon_{J,2l} - \epsilon_{J,2l+1}).\tag{2.16}$$

The $\tilde{\epsilon}_{j,k}$ are called father function coefficients (FFC). Thus, the difference between $\epsilon_{J,l}$ and $\epsilon^{J-1}(x)$ is given by an FFC term as

$$\tilde{\epsilon}^{J-1}(x) \equiv \sum_{l=0}^{2^{J-1}-1} \tilde{\epsilon}_{J-1,l} \psi_{J-1,l}^H(x).\tag{2.17}$$

Eq.(2.15) becomes then

$$\epsilon^J(x) = \epsilon^{J-1}(x) + \tilde{\epsilon}^{J-1}(x)\tag{2.18}$$

The term $\tilde{\epsilon}^{J-1}(x)$ contains all information lost during the window smoothing from order J to $J-1$. While not immediately obvious, these two functions, the mother functions and the father functions, together form a compactly supported orthogonal bases.

2.2 Multiresolution analysis

Eq.(2.18) shows that the J -th distribution can be resolved into a $(J-1)$ -th smoothed distribution and a term given by $(J-1)$ -th FFCs. We can repeat this procedure, i.e. resolving the $(J-1)$ -th distribution into $(J-2)$ -th smoothed distribution and a term containing the $(J-2)$ -th FFCs, and so on. The original distribution $\epsilon(x)$ can then be resolved scale by scale as

$$\begin{aligned}\epsilon^J(x) &= \epsilon^{J-1}(x) + \tilde{\epsilon}^{J-1}(x) \\ &= \epsilon^{J-2}(x) + \tilde{\epsilon}^{J-2}(x) + \tilde{\epsilon}^{J-1}(x) \\ &\dots \\ &= \epsilon^0(x) + \tilde{\epsilon}^0(x) + \dots + \tilde{\epsilon}^{J-2}(x) + \tilde{\epsilon}^{J-1}(x)\end{aligned}\tag{2.19}$$

where

$$\epsilon^j(x) = \epsilon^0(x) + \tilde{\epsilon}^0(x) + \dots + \tilde{\epsilon}^{j-1}(x) = \sum_{l=0}^{2^j-1} \epsilon_{j,l} \phi_{j,l}^H(x)\tag{2.20}$$

and

$$\tilde{\epsilon}^j(x) \equiv \sum_{l=0}^{2^j-1} \tilde{\epsilon}_{j,l} \psi_{j,l}^H(x).\tag{2.21}$$

Eq.(2.19) is a wavelet multiscale decomposition (or wavelet multiresolution analysis) of $\epsilon(x)$. As emphasized before, unlike the window function decomposition ($\epsilon^j(x)$), the wavelet multiscale decomposition ($\epsilon^j(x)$ and $\tilde{\epsilon}^j(x)$) does not lose information. In other words, one cannot reconstruct $\epsilon(x)$ from windowed components $\epsilon^j(x)$, ($j = 0, 1, \dots, J-1$), but we are able to reconstruct the original distribution from the “difference” functions $\tilde{\epsilon}^j(x)$, ($j = 0, 1, \dots, J-1$), and $\epsilon^0(x)$. Here $\epsilon^0(x) = \epsilon_{0,0}\phi_{0,0}^H(x)$, and $\epsilon_{0,0}$ is simply the mean density of the distribution $\epsilon(x)$ in the range $[0, L]$. Using (2.1), we have $\epsilon^0(x) = 0$.

Moreover, the father functions $\psi_{j,l}^H(x)$ are orthogonal with respect to *both* indexes j and l , i.e.

$$\int_0^L \psi_{j',l'}^H(x) \psi_{j,l}^H(x) dx = \left(\frac{L}{2^j}\right) \delta_{j',j} \delta_{l',l} \quad (2.22)$$

where $\delta_{j',j}$ is the Kronecker delta. For a given j , $\psi_{j,l}^H(x)$ are also orthogonal to mother functions $\phi_{j',l}^H(x)$ with $j' \leq j$, i.e.

$$\int_0^L \phi_{j',l'}^H(x) \psi_{j,l}^H(x) dx = 0, \quad \text{if } j' \leq j. \quad (2.23)$$

The FFCs in eq.(2.21) can be found by

$$\tilde{\epsilon}_{j,l} = \frac{2^j}{L} \int_0^L \epsilon(x) \psi_{j,l}^H(x) dx. \quad (2.24)$$

The last line of Eq.(2.19) is then

$$\begin{aligned} \epsilon(x) = \epsilon^J(x) &= \epsilon^0(x) + \tilde{\epsilon}^0(x) + \dots + \tilde{\epsilon}^{J-2}(x) + \tilde{\epsilon}^{J-1}(x) \\ &= \sum_{j=0}^{J-1} \sum_{l=0}^{2^j-1} \tilde{\epsilon}_{j,l} \psi_{j,l}^H(x). \end{aligned} \quad (2.25)$$

The FFCs provide a complete representation of $\epsilon(x)$ which we will call the Haar representation.

2.3 Compactly supported orthogonal bases

The Haar representation suffers from the drawback that the $\psi_{j,l}^H(x)$ are not localized in Fourier space. As was mentioned in §2, an adequate space-scale decomposition should be localized in both physical and scale (Fourier) space. The top-hat window function (2.6) and the wavelet (2.10) cannot meet this condition, because they are discontinuous. In the mid-80's to early 90's a great deal of work was done in trying to find a continuous bases that was well localized in Fourier space (Daubechies 1988, Meyer 1988, Mallat 1989, Mallat & Zhong 1990,). Specifically, Daubechies (1988) constructed several families of wavelets and scaling functions which are orthogonal, have compact support and are continuous.

In order to construct a compactly supported discrete wavelets basis the following two recursive equations were involved (Daubechies 1992, Meyer 1993).

$$\begin{aligned} \phi(\eta) &= \sum_l a_l \phi(2\eta - l) \\ \psi(\eta) &= \sum_l b_l \phi(2\eta + l) \end{aligned} \quad (2.26)$$

It is easy to show that the Haar scaling (2.6) and wavelet (2.12) satisfy eq.(2.26) only if the coefficients $a_0 = a_1 = b_0 = -b_1 = 1$ are nonvanishing.

Directly integrating the first equation in (2.26) it follows that

$$\sum_l a_l = 2. \quad (2.27)$$

Requiring orthonormality for $\phi(x)$ with respect to discrete integer translations, i.e.

$$\int_{-\infty}^{\infty} \phi(\eta - m)\phi(\eta)d\eta = \delta_{m,0}, \quad (2.28)$$

we have that

$$\sum_l a_l a_l + 2m = 2\delta_{0,m}. \quad (2.29)$$

The wavelet $\psi(\eta)$ has to qualify as a “difference” function, i.e. it is admissible. We have then

$$\int_{-\infty}^{+\infty} \psi(\eta)d\eta = 0, \quad (2.30)$$

so we need

$$\sum_l b_l = 0 \quad (2.31)$$

The multiresolution analysis requires that

$$\int_{-\infty}^{\infty} \psi(\eta)\phi(\eta - l)d\eta = 0. \quad (2.32)$$

So one has

$$b_l = (-1)^l a_{1-l}. \quad (2.33)$$

After the Haar wavelet, the simplest solution of the recursive equations (2.26) with conditions (2.27), (2.29) is

$$a_0 = (1 + \sqrt{3})/4, \quad a_1 = (3 + \sqrt{3})/4, \quad a_2 = (3 - \sqrt{3})/4, \quad a_3 = (1 - \sqrt{3})/4. \quad (2.34)$$

This is called the Daubechies 4 wavelet (D4) and is plotted in Figure 2. In general, the more coefficients a_l that are nonvanishing, the wider the compact support is, while the wavelet itself becomes smoother (Daubechies 1992; Chui 1992; Kaiser, 1994)

2.4 DWT decomposition

To conduct a DWT analysis, one first constructs the DWT bases by dilation and translation of $\phi(x)$ and $\psi(x)$ as

$$\phi_{j,l}(x) = \left(\frac{2^j}{L}\right)^{1/2} \phi(2^j x/L - l) \quad (2.35)$$

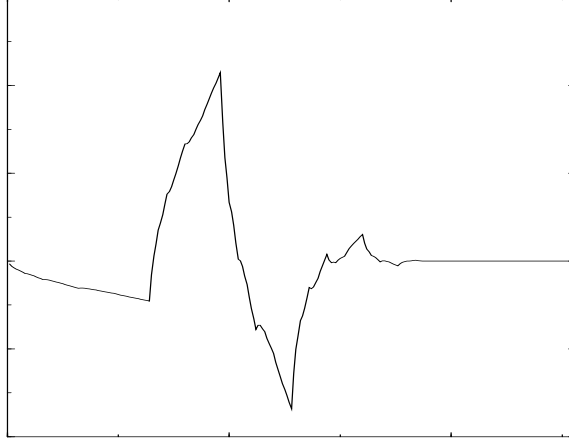


Figure 2: The Daubechies 4 wavelet, $\psi(\eta)$, determined by (2.34). The wavelet is plotted for presentation purposes only, so the units are arbitrary.

and

$$\psi_{j,l}(x) = \left(\frac{2^j}{L}\right)^{1/2} \psi(2^j x/L - l), \quad (2.36)$$

where $\psi_{j,l}$ and $\phi_{j,l}$ with integer j and l are the father functions and mother functions, respectively. Different from eqs.(2.7) and (2.13), eqs.(2.35) and (2.36) include a normalization factor $(2^j/L)^{1/2}$. The set of $\psi_{j,l}$ and $\phi_{0,m}(x)$ with $0 \leq j < \infty$ and $-\infty < l, m < \infty$ form a complete, orthonormal basis in the space of functions with period length L .

To subject a finite sample in region L to a DWT expansion, we introduce an auxiliary density distribution $\rho(x)$ which is an L periodic function defined on space $-\infty < x < \infty$. Using the complete, orthonormal basis, $\psi_{j,l}$ and $\phi_{j,m}(x)$, the density distribution $\rho(x)$ can be expanded as

$$\rho(x) = \sum_{m=-\infty}^{\infty} c_{0,m} \phi_{0,m}(x) + \sum_{j=0}^{\infty} \sum_{l=-\infty}^{\infty} \tilde{c}_{j,l} \psi_{j,l}(x) \quad (2.37)$$

where the coefficients $c_{0,m}$ and $\tilde{c}_{j,l}$ are calculated by the inner products

$$c_{0,m} = \int_{-\infty}^{\infty} \rho(x) \phi_{0,m}(x) dx, \quad (2.38)$$

and

$$\tilde{c}_{j,l} = \int_{-\infty}^{\infty} \rho(x) \psi_{j,l}(x) dx. \quad (2.39)$$

Because all bases functions $\int_{-\infty}^{\infty} \psi_{j,l}(x) dx = 0$ [eq.(2.30)], eq.(2.37) can be rewritten as

$$\rho(x) = \sum_{m=-\infty}^{\infty} c_{0,m} \phi_{0,m}(x) + \bar{\rho} \sum_{j=0}^{\infty} \sum_{l=-\infty}^{\infty} \tilde{\epsilon}_{j,l} \psi_{j,l}(x) \quad (2.40)$$

where $\bar{\rho}$ is the mean density, and

$$\tilde{\epsilon}_{j,l} = \int_{-\infty}^{\infty} \epsilon(x) \psi_{j,l}(x) dx \quad (2.41)$$

where $\epsilon(x) = (\rho(x) - \bar{\rho})/\bar{\rho}$ is the density contrast as eq.(2.1).

By definition, $\rho(x) = \rho(x + mL)$ for integers m , eq.(2.38) can be rewritten as

$$c_{0,m} = \int_{-\infty}^{\infty} \rho(x + mL) \phi_{0,m}(x) dx. \quad (2.42)$$

Using eq.(2.35), we have then

$$\begin{aligned} c_{0,m} &= \int_{-\infty}^{\infty} \rho(x + mL) L^{-1/2} \phi(x/L - m) dx \\ &= \int_{-\infty}^{\infty} \rho(x') L^{-1/2} \phi(x'/L) dx' \\ &= \int_{-\infty}^{\infty} \rho(x') \phi_{0,0}(x') dx' = c_{0,0} \end{aligned} \quad (2.43)$$

where $x' = x + mL$. The coefficients $c_{0,m}$ are independent of m . Using the property of “partition of unity” of the scaling function (Daubechies 1992)

$$\sum_{m=-\infty}^{\infty} \phi(\eta + m) = 1, \quad (2.44)$$

from eq.(2.43) one has

$$\begin{aligned} c_{0,0} &= \int_{-\infty}^{\infty} \rho(x) L^{-1/2} \phi(x/L) dx \\ &= \sum_{m=-\infty}^{\infty} \int_0^L \rho(x + mL) L^{-1/2} \phi(x/L + m) dx \\ &= L^{-1/2} \int_0^L \rho(x) \sum_{m=-\infty}^{\infty} \phi(x/L + m) dx \\ &= L^{-1/2} \int_0^L \rho(x) dx. \end{aligned} \quad (2.45)$$

The first term in the expansion (2.40) becomes

$$\sum_{m=-\infty}^{\infty} c_{0,m} \phi_{0,m}(x) = c_{0,0} L^{-1/2} \sum_{m=-\infty}^{\infty} \phi(x/L + m) = L^{-1} \int_0^L \rho(x) dx. \quad (2.46)$$

This term is the mean density $\bar{\rho}$. From eq.(2.40) we have finally

$$\epsilon(x) = \frac{\rho(x) - \bar{\rho}}{\bar{\rho}} = \sum_{j=0}^{\infty} \sum_{l=-\infty}^{\infty} \tilde{\epsilon}_{j,l} \psi_{j,l}(x) \quad (2.47)$$

where the father function coefficients $\tilde{\epsilon}_{j,l}$ are given by eq.(2.41). Eq.(2.47) has the same terms as eq.(2.25), and is a multiresolution analysis with respect to the orthogonal bases $\psi_{j,l}(x)$.

While the multiresolution analysis eq.(2.19) still holds, eqs.(2.20) and (2.21) should be replaced by

$$\epsilon^j(x) = \tilde{\epsilon}^0(x) + \tilde{\epsilon}^1(x) \dots + \tilde{\epsilon}^{j-1}(x) = \sum_{l=0}^{2^j-1} \epsilon_{j,l} \phi_{j,l}(x) \quad (2.48)$$

and

$$\tilde{\epsilon}^j(x) \equiv \sum_{l=0}^{2^j-1} \tilde{\epsilon}_{j,l} \psi_{j,l}(x). \quad (2.49)$$

2.5 Relationship between Fourier and DWT expansion

In terms of the Fourier transform, $\epsilon(x)$ is expressed as

$$\epsilon(x) = \sum_{n=-\infty}^{\infty} \epsilon_n e^{i2\pi nx/L} \quad (2.50)$$

with the coefficients computed by

$$\epsilon_n = \frac{1}{L} \int_0^L \epsilon(x) e^{-i2\pi nx/L} dx. \quad (2.51)$$

Since both the DWT and Fourier bases sets are complete, a function may be represented by either bases and there is thus a relationship between the FFCs and the Fourier coefficients. Substituting expansion (2.50) into eq.(2.41), yields

$$\tilde{\epsilon}_{j,l} = \sum_{n=-\infty}^{\infty} \epsilon_n \int_{-\infty}^{\infty} e^{i2\pi nx/L} \psi_{j,l}(x) dx = \sum_{n=-\infty}^{\infty} \epsilon_n \hat{\psi}_{j,l}(-n) \quad (2.52)$$

where $\hat{\psi}_{j,l}(n)$ is the Fourier transform of $\psi_{j,l}(x)$, i.e.

$$\hat{\psi}_{j,l}(n) = \int_{-\infty}^{\infty} \psi_{j,l}(x) e^{-i2\pi nx/L} dx. \quad (2.53)$$

Using eq.(2.36), eq.(2.52) gives

$$\tilde{\epsilon}_{j,l} = \sum_{n=-\infty}^{\infty} \left(\frac{2^j}{L} \right)^{1/2} \epsilon_n \int_{-\infty}^{\infty} e^{i2\pi nx/L} \psi(2^j x/L - l) dx. \quad (2.54)$$

Defining variable $\eta = 2^j x/L - l$, one finds

$$\tilde{\epsilon}_{j,l} = \sum_{n=-\infty}^{\infty} \left(\frac{2^j}{L} \right)^{-1/2} \epsilon_n e^{i2\pi nl/2^j} \int_{-\infty}^{\infty} e^{i2\pi n\eta/2^j} \psi(\eta) d\eta \quad (2.55)$$

or

$$\tilde{\epsilon}_{j,l} = \sum_{n=-\infty}^{\infty} \left(\frac{2^j}{L} \right)^{-1/2} \epsilon_n \hat{\psi}(-n/2^j) e^{i2\pi nl/2^j} \quad (2.56)$$

where $\hat{\psi}(n)$ is the Fourier transform of the wavelet $\psi(\eta)$

$$\hat{\psi}(n) = \int_{-\infty}^{\infty} \psi(\eta) e^{-i2\pi n\eta} d\eta. \quad (2.57)$$

Eq.(2.56) is the expression of the FFCs in terms of the Fourier coefficients.

From expansions (2.51) and (2.49), one can also express the Fourier coefficient, ϵ_n , in terms of FFCs as (see Appendix A)

$$\epsilon_n = \frac{1}{L} \sum_{j=0}^{\infty} \sum_{l=0}^{2^j-1} \tilde{\epsilon}_{j,l} \hat{\psi}_{j,l}(n), \quad n \neq 0 \quad (2.58)$$

or

$$\epsilon_n = \sum_{j=0}^{\infty} \sum_{l=0}^{2^j-1} \left(\frac{1}{2^j L} \right)^{1/2} \tilde{\epsilon}_{j,l} e^{-i2\pi nl/2^j} \hat{\psi}(n/2^j), \quad n \neq 0. \quad (2.59)$$

Eq.(2.58) and (2.59) show how the Fourier coefficients are determined by a DWT analysis.

2.6 Comparison with the Fourier transform

The difference between the Fourier transform and the DWT can easily be seen in phase space (x, k) . According to the uncertainty principle, each mode of a complete, orthogonal bases set corresponds to a "element" with size Δx and Δk , and area $\Delta x \Delta k \sim 2\pi$ in phase space. For the Fourier transform, the "elements" are taken to be $\Delta k = 0$ and $\Delta x = \infty$, while for the DWT both Δk and Δx are finite, and $\Delta x \Delta k \simeq 2\pi$ (Figure 3).

The representation by the Fourier bases, i.e., the trigonometric functions, is delocalized ($\Delta x = \infty$). The DWT resolves the distribution $\epsilon(x)$ simultaneously in terms of its standard variable (say space) and its conjugate counterpart in Fourier space (wavenumber or scale) up to the limit of uncertainty principle.

This doesn't mean that the Fourier transform loses information about $\epsilon(x)$ but rather that the information on the position is spread out. For instance, let us consider a distribution that contains a few clumps of scale d . The positions of the clumps are related to the phases of all the Fourier coefficients $k < 2\pi/d$. There is no way to find the positions of the clumps from a finite number of Fourier coefficients. The only solution would be to reconstruct $\epsilon(x)$ from *all* the Fourier coefficients. If some of the "clumps" are due to experimental errors, we will not be able to filter them out because they have affected all the Fourier coefficients.

On the other hand, the DWT keeps the locality present in the distribution and allows for the local reconstruction of a distribution. It is then possible to reconstruct only a portion of it. There is a relationship between the local behavior of a distribution and the local behavior of its FFCs. For instance, if a distribution $\epsilon(x)$ is locally smooth, the corresponding FFCs will remain small, and if $\epsilon(x)$ contains a clump, then in its vicinity the FFCs amplitude will increase drastically. To reconstruct a portion of the distribution, it is only necessary to consider the FFCs belonging to the

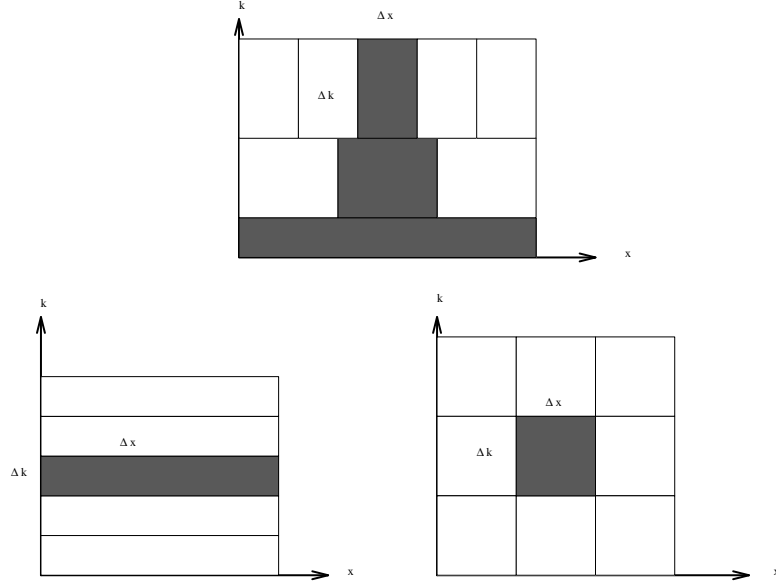


Figure 3: “Element” of different transforms in phase space (x, k) . A. DWT, both Δk and Δx are finite, and $\Delta x \Delta k \simeq 2\pi$. B. Fourier transform, the “elements” are $\Delta k = 0$ and $\Delta x = \infty$. C. Gabor transform, here $\Delta k = \Delta x = \text{constant}$, regardless the scale.

corresponding subdomain of the wavelet space (j, l) . If the FFCs are occasionally subject to errors, this will only affect the reconstructed distribution locally near the flawed positions. Furthermore, the Fourier transform is also particularly sensitive to phase errors due to the alternating character of the trigonometric series. This is not the case for the DWT.

Early approaches to finding information on the locations in the Fourier transform schemes were given by the Wigner function in quantum mechanics and the Gabor transform. The difference between the Gabor transform and the DWT can also be seen in Figure 3. The orthogonal basis of the DWT are obtained by (space) translation and (scale) dilation of one wavelet. The DWT transform gives very good spatial resolution on small scales, and very good scale resolution on large scales. Gabor’s windowed Fourier transform is based on a family of trigonometric functions exhibiting increasingly many oscillations in a window of constant size. In this case the spatial resolution on small scales and the range on large scales are limited by the size of the window.

The relation between the discrete and the continuous Fourier transforms when $\epsilon(x)$ is viewed as a continuous distribution sampled on an interval Δ is $\hat{\epsilon}(n) = \Delta \hat{\epsilon}_n$ where $\hat{\epsilon}(n)$ is the usual continuous Fourier transform and $\hat{\epsilon}_n$ is the discrete Fourier transform. However, no such relationship exists between the discrete wavelet transform, such as the D4 wavelet, and the continuous wavelet transform (CWT). The D4 wavelet has no continuous analog. Each type of complete, orthogonal wavelet bases must be constructed from scratch. In general, CWTs form an over complete bases, i.e. they are highly redundant. As a consequence, CWT coefficients of a random sample show A

correlation that is not in the sample itself but is given by the over complete bases. Since the DWT is complete and orthogonal, this is not a problem in using the DWT. The point is that the difference between the DWT and the CWT is essential, and by construction, these two bases are very different.

The DWT is not intended to replace the Fourier transform, which remains very appropriate in the study of all topics where there is no need for local information.

3 A DWT Estimation of the Probability Distribution Function

3.1 One-point distribution of FFCs

As has been emphasized in §1, the statistical features of a non-linearly evolved density field can not be completely described by the power spectrum or the two-point correlation function. For a complete description of salient statistical features, the probability distribution functions (PDF) of the density field are required.

There is, however, a very real problem in determining the PDF due mainly to the central limit theorem of random fields (Adler 1981). If the universe consists of a large number of randomly distributed clumps with a non-Gaussian one-point function, eq.(2.51) shows that for large L the Fourier amplitudes, ϵ_n , are given by a superposition of a large number of non-Gaussian clumps. According to the central limit theorem, the distribution of ϵ_n will be Gaussian when the total number of clumps is large. Thus, in general, the statistical features of the clumps can not be seen from the one-point distribution of the Fourier modes, ϵ_n , even if the PDF function of clumps is highly non-Gaussian. If the clumps are not distributed independently, but are correlated, the central limit theorem still holds if the two-point correlation function of the clumps approaches zero sufficiently fast (Fan & Bardeen 1995).

On the other hand, the father functions, $\psi_{j,l}(x)$, are localized. If the scale of the clump is d , eq.(2.41) shows that the FFC, $\tilde{\epsilon}_{j,l}$, with $j = \log_2(L/d)$, is determined only by the density field in a range containing no more than one clump. That is, for scale j the FFCs are not given by a superposition of a large number of the clumps, but determined by at most one of them. Thus, the one point distribution of the FFC, $\tilde{\epsilon}_{j,l}$, avoids the restriction of the central limit theorem, and is able to detect the PDF related to the clumps, regardless the total number of the clumps in the sample being considered.

This point can also be shown from the orthonormal bases being used for the expansion of the density field. A key condition needed for the central limit theorem to hold is that the modulus of the bases be less than C/\sqrt{L} , where L is the size of the sample and C is a constant (Ivanov & Leonenko 1989). Obviously, all Fourier-related orthonormal bases satisfy this condition because the Fourier orthonormal bases in 1-dimension are such that $(1/\sqrt{L})|\sin kx| < C/\sqrt{L}$ and $(1/\sqrt{L})|\cos kx| < C/\sqrt{L}$, and C is independent of coordinates in both physical space x and scale space k . On the

other hand, the father functions (2.36) have

$$|\psi_{j,l}(x)| \sim \left(\frac{2^j}{L}\right)^{1/2} O(1) \quad (3.1)$$

because the magnitude of the basic wavelet $\psi(x)$ is of the order 1 [eq.(3.26)]. The condition $|\psi_{j,l}(x)| < C/\sqrt{L}$, will no longer hold for a constant C independent of scale variable j .

3.2 “Ensemble” of FFCs

In cosmology, no ensemble of cosmic density fields exists, and at most only one realization, i.e. the observed density distribution, is available. In order to have reasonable statistics, the cosmic density field is usually assumed to be ergodic: the average over an ensemble is equal to the spatial average taken over one realization. It is sometimes called the “fair sample hypothesis” in LSS study (Peebles 1980). A homogeneous Gaussian field with continuous spectrum is certainly ergodic (Adler 1981). In some non-Gaussian cases, such as homogeneous and isotropic turbulence (Vanmarke, 1983), ergodicity also approximately holds. Roughly, the ergodic hypothesis is reasonable if spatial correlations are decreasing sufficiently rapidly with increasing separation. The volumes separated with distances larger than the correlation length are approximately statistically independent. Even for one realization of $\epsilon(x)$, FFCs at different locations l can be treated as results from statistically independent realizations. Thus, the values of $\epsilon_{j,l}$ on different l form an ensemble of the FFCs on scale j .

This result can be more clearly seen from eq.(2.56). For many wavelets, their Fourier transforms $\hat{\psi}(n)$ are non-zero (localized) in two narrow ranges centered at $n = \pm n_p$. For instance, the Battle-Lemarié wavelet $n_p = \pm 1$, and the Daubechies 4 wavelet $n_p \sim \pm 1.9$. The sum over n in eq.(2.56) is only taken over the two ranges $(n_p - 0.5\Delta n_p)2^j \leq n \leq (n_p + 0.5\Delta n_p)2^j$ and $-(n_p + 0.5\Delta n_p)2^j \leq n \leq -(n_p - 0.5\Delta n_p)2^j$, where Δn_p is the width of the non-zero ranges of $\hat{\psi}(n)$. Eq.(2.56) can then be approximately rewritten as

$$\begin{aligned} \tilde{\epsilon}_{j,l} &\simeq \left(\frac{L}{2^j}\right)^{1/2} 2 \sum_{n=(n_p-0.5\Delta n_p)2^j}^{(n_p+0.5\Delta n_p)2^j} \text{Re}\{\hat{\psi}(n_p)\epsilon_n e^{i2\pi nl/2^j}\} \\ &\simeq \left(\frac{L}{2^j}\right)^{1/2} |\hat{\psi}(n_p)| 2 \sum_{n=(n_p-0.5\Delta n_p)2^j}^{(n_p+0.5\Delta n_p)2^j} |\epsilon_n| \cos(\theta_\psi + \theta_n + 2\pi nl/2^j) \end{aligned} \quad (3.2)$$

where we have used $\hat{\psi}(-n_p) = \hat{\psi}^*(n_p)$ and $\epsilon_{-n} = \epsilon_n^*$, because both $\psi(x)$ and $\epsilon(x)$ are real. θ_ψ, θ_n in eq.(9) are the phases of $\hat{\psi}(n_p)$ and ϵ_n , respectively.

As we pointed out in §3.1, ϵ_n is Gaussian even when the clumps are non-Gaussian. For a homogeneous random field, the phase of ϵ_n , i.e. θ_n , should be uniformly randomly distributed and from eq.(3.2), the probability distribution of $\tilde{\epsilon}_{j,l}$ is independent of l . Thus, each FFC is a realization of the l – *independent* stochastic variable $\tilde{\epsilon}_{j,l}$. The FFCs, $\tilde{\epsilon}_{j,l}$, on scale j form an ensemble with 2^j

realizations. The statistics with respect to the one-point distribution of FFCs $\tilde{\epsilon}_{j,l}$ should be equal to the results of the ensemble statistics. The goodness of this estimation can be measured by the Large Number Theorem, that is, the relative error is about $1/\sqrt{2^j}$. Simply stated, when the “fair sample hypothesis” holds, the one-point distribution of FFCs from (observed) one-realization will be a fair estimate of the PDF of the cosmic density field.

3.3 Scale mixing

The PDF is sometimes measured by the count in cell (CIC) method. The CIC detects the one-point distribution of the density field in given cubical cells with side d or Gaussian spheres with radius R_G . It is generally believed that the CIC one-point distribution of window d is dominated by the density fluctuations on scale $\sim 2d$ or R_G .

Actually, the CIC analysis is essentially the same as the MFC. The window function of the CIC corresponds to the mother function, and the count to the amplitude of the MFCs. The one-point distribution given by the CIC have similar properties as the MFC one-point distribution. A problem with the MFC one-point distributions is scale mixing. Even though the mother functions of the DWT, $\phi_{j,l}(x)$, are localized in spatial space they are not orthogonal with respect to the scale index j , i.e. not localized in Fourier space. The MFCs, $\phi_{j,l}(x)$, are dependent on perturbations on all scales larger than $L/2^j$. Thus, if the clumps are multiscaled, the MFCs will also be Gaussian as required by the central limit theorem and the MFC one-point distribution may miss the clumps. Similarly, the CIC is scale mixed, and not suitable for studying the scale dependence (or spectrum) of various statistical measures.

There are more problem related to the cubic cell CIC. The cubic cell window is just the Haar wavelet or Daubechies 2 (D2) [see eq.(2.5)]. It is very well known that among Daubechies wavelets, only D2 is not localized in Fourier space because the Fourier transform of its wavelet (2.12) is

$$\hat{\psi}^H(n) = \frac{2}{\pi n} [\sin(\pi n) - i \cos(\pi n)] \sin^2(\pi n/2) \quad (3.3)$$

When $n \ll 1$, $\hat{\psi}^H(n) \sim -i(\pi/2)n$. Therefore, eq.(2.56) gives

$$\tilde{\epsilon}_{j,l} = \sum_{n < 2^j} \left(\frac{2^j}{L} \right)^{-1/2} \epsilon_n \frac{i\pi A n}{2^{j+1}} e^{i2\pi n l/2^j} + \text{terms } n \geq 2^j \quad (3.4)$$

Eq.(3.4) shows that the large scale (small n) perturbations will significantly contribute to, and even dominate the $\epsilon_{j,l}$ if $\lim_{n \rightarrow 0} n\epsilon$ is larger than a non-zero constant. So even the FFC one-point distributions of the D2 wavelet are not a good way of measuring the PDF.

3.4 Spectrum of FFC cumulants

Since FFC one-point distributions effectively allow for scale decomposition, one can easily calculate the spectrum of the FFC moments or cumulants on any order as follows.

The second order cumulant is given by

$$\sigma_j^2 \equiv \frac{1}{2^j} \sum_{l=0}^{2^j-1} (\tilde{\epsilon}_{j,l} - \overline{\tilde{\epsilon}_{j,l}})^2, \quad (3.5)$$

where $\overline{\tilde{\epsilon}_{j,l}}$ is the average of $\tilde{\epsilon}_{j,l}$ over l . σ_j^2 is, in fact, the power spectrum with respect to the modes of DWT (see, §4.1).

The third and fourth orders are

$$C_j^3 \equiv \frac{1}{2^j} \sum_{l=0}^{2^j-1} (\tilde{\epsilon}_{j,l} - \overline{\tilde{\epsilon}_{j,l}})^3, \quad (3.6)$$

$$C_j^4 \equiv \frac{1}{2^j} \sum_{l=0}^{2^j-1} (\tilde{\epsilon}_{j,l} - \overline{\tilde{\epsilon}_{j,l}})^4 - 3\sigma_j^4, \quad (3.7)$$

C_j^3 and C_j^4 will measure the spectra of skewness and kurtosis, respectively (see, §5.1).

Generally, the spectrum of n -th order moment is defined as

$$C_j^n \equiv \frac{1}{2^j} \sum_{l=0}^{2^j-1} (\tilde{\epsilon}_{j,l} - \overline{\tilde{\epsilon}_{j,l}})^n, \quad (3.8)$$

The definitions (3.5) - (3.8) show that the numerical work of calculating higher order moments (cumulant) is not any more difficult than calculating the second order moments. Generally, the calculation of third and higher order correlations of large scale structure samples is very strenuous work. But the numerical work involved in calculating the DWT is not more difficult than the FFT, and can be faster. The FFT requires $\sim N \log N$ calculations, while the DWT, using a “pyramid” scheme, requires only order N calculations (Press et al. 1992).

4 Local power spectrum

4.1 Power Spectrum with respect to DWT basis

For the Fourier expansion (2.50) and (2.51) Parseval's theorem is

$$\frac{1}{L} \int_0^L |\epsilon(x)|^2 dx = \sum_{n=-\infty}^{\infty} |\epsilon_n|^2, \quad (4.1)$$

which shows that the perturbations can be decomposed into domains, n , by the orthonormal Fourier basis functions. The power spectrum of perturbations on length scale L/n is then defined as

$$P(n) = |\epsilon_n|^2. \quad (4.2)$$

Similarly, the Parseval theorem for the expansion (2.49) can be shown to be (see Appendix B)

$$\frac{1}{L} \int_0^L |\epsilon(x)|^2 dx = \sum_{j=0}^{\infty} \frac{1}{L} \sum_{l=0}^{2^j-1} |\tilde{\epsilon}_{j,l}|^2. \quad (4.3)$$

Comparing eqs.(3.3) and (3.1), one can relate the term $\sum_{l=0}^{2^j-1} |\tilde{\epsilon}_{j,l}|^2 / L$ to the power of perturbations on length scale $L/2^j$, and the term $|\tilde{\epsilon}_{j,l}|^2 / L$ to the power of the perturbation on scale $L/2^j$ at position $lL/2^j$. The spectrum with respect to the DWT bases can be defined as

$$P_j = \frac{1}{L} \sum_{l=0}^{2^j-1} |\tilde{\epsilon}_{j,l}|^2. \quad (4.4)$$

The DWT spectrum should be defined as the variance of the FFCs, i.e.,

$$P_j^{var} = \frac{1}{L} \sum_{l=0}^{2^j-1} (\overline{\tilde{\epsilon}_{j,l}} - \tilde{\epsilon}_{j,l})^2. \quad (4.5)$$

Because the mean of the FFCs, $\overline{\tilde{\epsilon}_{j,l}}$, over l is zero [eq.(2.56)], P_j should be equal to P_j^{var} . Comparing with eq.(3.5), we have $\sigma_j^2 = (L/2^j)P_j^{var}$.

4.2 Relationship between Fourier and DWT Spectra

The relationship between the spectra of the Fourier expansion (4.2) and the DWT (4.4) or (4.5) can be found from eq.(3.2), which shows that the FFCs on scale j are mainly determined by the Fourier components ϵ_n , with n centered at

$$n = \pm n_p 2^j, \quad (4.6)$$

where $|n_p|$ are the positions of the peaks of $\hat{\psi}(n)$. Thus, from eqs.(4.4), (4.5) and (4.6), we have

$$P(n)_j \simeq \frac{1}{2^{j+1}\Delta n_p} |\hat{\psi}(n_p)|^{-2} P_j^{var} \quad (4.7)$$

where $P(n)_j$ is the average of Fourier spectrum on the scale j given by

$$P(n)_j = \frac{1}{2^j \Delta n_p} \sum_{n=(n_p-0.5\Delta n_p)2^j}^{(n_p+0.5\Delta n_p)2^j} P(n). \quad (4.8)$$

Eqs. (4.7) and (4.8) provide the basic way of detecting the Fourier power spectrum by a DWT analysis.

From eqs.(4.8) and (4.6), one has

$$\log P(k)_j = \log P_j - (\log 2)j + A, \quad (4.9)$$

and

$$\log k = (\log 2)j - \log L/2\pi + B. \quad (4.10)$$

The factors A and B are given by

$$A = -\log(2\Delta n_p |\hat{\psi}(n_p)|^2) \quad (4.11)$$

and

$$B = \log n_p. \quad (4.12)$$

The constants A and B depend on the basic wavelet $\psi(\eta)$ being used in the DWT analysis. In the case of the D4 wavelet, $A = 0.602$, and $B = 0.270$.

Eqs.(4.9) - (4.12) provide the way of directly transferring a DWT spectrum P_j or P_j^{var} into the corresponding Fourier spectrum $P(k)_j$ and *vice versa*.

4.3 Finite size and complex geometry of samples

It is well known that a difficulty in spectrum detection comes from the finite size of the sample which leads to uncertainty in the mean density of the objects being considered. The classical spectrum estimator, i.e., the Fourier transform of the two-point correlation function depends essentially on the mean density $\bar{\rho}$. A two-point correlation analysis cannot detect any correlations with amplitude comparable to the uncertainty of the mean density. If we determine the spectrum via the two-point correlation function, the uncertainty in $\bar{\rho}$ leads to uncertainties on all scales in which the correlation amplitude is comparable to the uncertainty in the mean density. The problem of the uncertainty in the mean density is more severe for the study of high redshift objects because the mean density of these objects generally is redshift-dependent.

The CIC or Fourier transform on a finite domain have been used to avoid this difficulty. The CIC detects the variance of density fluctuations in windows of a cubical cell with side l or Gaussian sphere with radius R_G . The behavior of the perturbations on scales larger than the size of a sample is assumed not to play an important role. This reduces the uncertainties caused by a poor knowledge of long wavelength perturbations and by the finite size of the observational samples. It is believed that the variance in cell l is mainly dominated by the perturbation on scale $\sim 2l$ or R_G . Therefore, the variances are considered to be a measure of the power spectrum on scale l (Efstathiou et al 1990, Kaiser & Peacock 1991). Additionally, the Fourier transform on a finite domain (the Gabor transform, for instance) can also avoid the difficulty of the infinity of x .

As was mentioned in §3.3, the problem with the CIC statistic is that the variances obtained from the decomposition of cells with different size d are not independent. While it is still possible to reconstruct the power spectrum by $\sigma^2(l)$, the scale mixing leads to uncertainty. The scale mixing becomes a serious problem when the power law spectrum has a negative index. Moreover, the resulting errors are not easy to interpret because the errors for different d are also not independent.

The DWT provides a method to solve this problem. Actually, this problem is the same as trying to detect a *local* (finite range) spectrum. One of the motivations of developing DWT was to measure local spectra (Yamada and Ohkitani 1991, Farge 1992). Because the FFCs are localized, one can calculate local power spectrum using the FFCs related to the finite range being considered. The FFCs are determined by the difference of the MFCs in a localized neighborhood, i.e., by measuring the differences between the *local* mean densities. As a consequence, the mean density over length scales larger than the sample's size is not necessary in calculating the FFCs on scales equal to or less

than the size of data. The influence of the uncertainty of the mean density is significantly reduced by the FFC spectrum detection.

To avoid the difficulty of finite sized samples, specific boundary conditions are sometimes selected. For instance, N-body simulations always assume a periodic condition. Yet, the choice of boundary conditions may affect the spectrum detection. Again, father functions $\psi_{j,l}(x)$ are compactly supported, and the FFCs that are uncertain due to the boundary conditions are only the coefficients at the boundary, $\tilde{\psi}_{j,l_1}$ and $\tilde{\psi}_{j,l_2}$, where l_1 and l_2 are the positions of the 1-D boundary. The uncertainty due to the choice of boundary conditions will also be suppressed by the wavelet SSD. We illustrate this point by using different boundary conditions to find the spectrum. Figure 4 shows the local spectrum of sample in a finite area L with 512 bins, with boundary conditions A) periodic outside this range; B) zero outside this range. Excluding a small effect on the largest scale (i.e. the scale of the size of the sample), all the local spectra remain unchanged regardless of which boundary conditions is used.

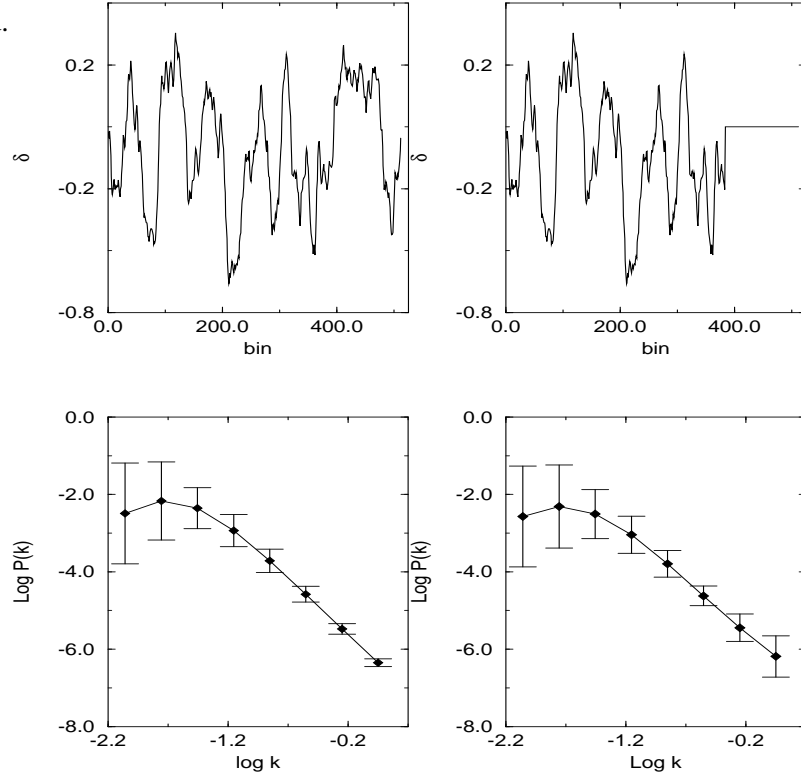


Figure 4: Density distributions generated from spectrum $P(k) = k/(1 + 10^5 k^4)$ in a range of $L = 512$ bins, where $k = 2\pi n/L$, and n is integer. The boundary conditions outside the 512 bin area are taken to be A) periodic, B) zero. C.) and D.) are the spectrum reconstruction for A.) and B.) respectively.

More precisely, the effect of boundary conditions on the FFCs should be described by the so-called “influence cone” which consists of the spatial support of all dilated father functions. For

instance, if $\psi_{jl}(x)$ is well-localized in the space interval Δx for $j = 0$, the influence cone centered at x_0 will be defined by $x \in [x_0 - (\Delta x/2^{j+1}), x_0 + (\Delta x/2^{j+1})]$. Namely, the FFCs corresponding to the positions with distance larger than $(\Delta x/2^{j+1})$ from the boundary will not be affected by the selection of boundary conditions.

This result is also useful in solving the problem of the complex geometry of observational data. For instance, samples of Ly α forests in QSO absorption spectra cover different spatial (redshift) ranges for different QSO's. Any statistic of a sample compiled from many QSO spectra needs, at the very least, a complicated weighting scheme. Moreover, the number density of Ly α forest lines depends on redshift, and therefore, it is very difficult to find a proper weighting scheme for methods which depends essentially on a good measure of the mean density of the sample. Despite the fact that samples of the Ly α clouds are relatively uniform among the various samples of high-redshift objects, and Ly α forest lines are numerous enough to provide statistical analysis, the power spectrum and higher order statistics of Ly α forests have not been systematically calculated because of the difficulty in trying to compensate for the geometry of the samples.

Since FFCs in the range being considered are not strongly affected by the data outside the range, one can freely extend a sample in spatial range (D_1, D_2) to a larger range (D_{min}, D_{max}) ($D_{min} < D_1, D_{max} > D_2$) by adding zero to the data in ranges (D_{min}, D_1) and (D_2, D_{max}) . One can then take statistics by simply dropping all FFCs related to the positions in the regions of (D_{min}, D_1) and (D_2, D_{max}) . Using this technique, all samples can be extended to a desired range (D_{min}, D_{max}) , and the geometrically complicated samples are regularized.

Local spectrum can also be detected by the Karhuen-Lo  ve (K-L) transform, or proper orthogonal decomposition, which is designed for an optimization over the set of orthogonal transformation of a covariance matrix. However, finding the K-L eigenvectors of a matrix of order f has computing complexity $O(f^3)$. In addition, the K-L bases are not admissible. Even after finding the eigenvectors of a data set, updating the bases with some extra samples will cost an additional $O(f^3)$ operations. On the other hand, the DWT can quasi-diagonalize the covariance matrix, and therefore, K-L transform can be approximately represented by wavelets which leads to less computing complexity (Wickerhauser 1994, Carruthers 1995).

5 Measures of non-Gaussianity

5.1 Spectra of skewness and kurtosis

For a density (contrast) distribution $\epsilon(x)$ in a range $L = N$ bins, the non-Gaussianity is usually measured by the skewness S and kurtosis K defined as

$$S \equiv \frac{1}{N\sigma^3} \sum_{i=1}^N (\epsilon(x_i) - \overline{\epsilon(x)})^3, \quad (5.1)$$

and

$$K \equiv \frac{1}{N\sigma^4} \sum_{i=1}^N [(\epsilon(x_i) - \overline{\epsilon(x_i)})^4] - 3. \quad (5.2)$$

These measures cannot describe any possible scale-dependence of the skewness and kurtosis.

Using the DWT, one can measure the non-Gaussianity by the spectrum of skewness defined as [see eqs.(3.6)]

$$S_j \equiv \frac{C_j^3}{\sigma_j^3} = \frac{1}{N_r 2^j \sigma_j^3} \sum_{s=1}^{N_r} \sum_{l=0}^{2^j-1} [(\tilde{\epsilon}_{j,l} - \overline{\tilde{\epsilon}_{j,l}})^3]_s, \quad (5.3)$$

and the spectrum of kurtosis as [eq.(3.7)]

$$K_j \equiv \frac{C_j^4}{\sigma_j^4} = \frac{1}{N_r 2^j \sigma_j^4} \sum_{s=1}^{N_r} \sum_{l=0}^{2^j-1} [(\tilde{\epsilon}_{j,l} - \overline{\tilde{\epsilon}_{j,l}})^4]_s - 3, \quad (5.4)$$

where the variance σ_j^2 is given by (3.5), and N_r is the number of samples. Unlike eqs.(5.1) and (5.2), the spectrum description eq.(5.3) and (5.4) can detect not only the non-Gaussianity of the density field, but also the scale of objects contributing to the non-Gaussian behavior.

Note that eqs.(5.3) and (5.4) differ slightly from usual definition of the skewness or kurtosis by the sum over s from 1 to N_r . This is because at small j one sample on the range L will yield only a small number of $\tilde{\epsilon}_{j,l}$, making the calculation of K_j meaningless. For instance, for $j = 2$, each sample gives only two FFCs, i.e. $\tilde{\epsilon}_{2,0}$ and $\tilde{\epsilon}_{2,1}$. In this case, $\overline{\tilde{\epsilon}_{j,l}} = (\tilde{\epsilon}_{2,0} + \tilde{\epsilon}_{2,1})/2$, and $K_j = -2$ if $N_r = 1$, regardless whether the sample is Gaussian or what wavelet function is used. The K_j for each sample can not be calculated separately and still have meaningful results at lower j . Generally, we have many samples covering the range L . One can compile subsets consisting of N_r samples. The number of $\tilde{\epsilon}_{j,l}$ will then be N_r times larger than one sample making the statistics at small j viable. As with the usual definitions of skewness and kurtosis, S_j and K_j should vanish for a Gaussian distribution.

5.2 Distribution of clumps

The effectiveness in detecting the scales of non-Gaussian objects can be illustrated by clump and valley structures. Let us consider non-Gaussian density fields consisting of clumps randomly distributed in a white noise background. Clump distributions are often used to test methods of detecting non-Gaussianity in large scale structure study (Perivolaropoulos 1994, Fan & Bardeen 1995). It has been shown that one cannot detect the non-Gaussianity of samples by the one-point probabilities of the individual Fourier modes, even when the samples contain only a few independent clumps (Kaiser & Peacock 1991).

To begin, first note that a clump or valley with density perturbation $\Delta\rho_c$ on length scale d at position l can be described as

$$\rho^\pm(x) = \begin{cases} \pm\Delta\rho_c & \text{if } lL/2^{J_c} \leq x < (l+1)L/2^{J_c} \\ 0 & \text{otherwise} \end{cases} \quad (5.5)$$

where $J_c = \log_2(L/d)$, and the positive and negative signs are for a clump and a valley, respectively. If a density field $\rho(x)$ consist of N randomly distributed clumps and valleys of scale d , so that the number density is $N/2^{J_c}d$ on average, the field can be realized by a random variable $\delta\rho$ with a probability distribution $P[\delta\rho \leq X]$ defined as

$$P[x \leq X] = \begin{cases} 0 & \text{if } X < -\Delta\rho_c \\ N/2^{J_c+1} & \text{if } -\Delta\rho_c < X < 0 \\ 1 - N/2^{J_c} & \text{if } 0 < X < \Delta\rho_c \\ 1 & \text{if } X > \Delta\rho_c \end{cases} \quad (5.6)$$

The distribution function $\delta\rho$ of clumps and valleys, $f_c(\delta\rho)$ can then be written approximately as

$$f_c(x) = \frac{dP}{dx} = (1 - \frac{N}{2^{J_c}})\delta(x) + \frac{N}{2^{J_c+1}}\delta(x - \Delta\rho_c) + \frac{N}{2^{J_c+1}}\delta(x + \Delta\rho_c). \quad (5.7)$$

The $\delta(\cdot)$ on the right hand side of eq.(5.7) denote Dirac δ -functions. The characteristic function of the random variable $\delta\rho$ of clumps and valleys is

$$\phi_c(u) = \int_{-\infty}^{\infty} f_c(x)e^{ixu}dx = \frac{2^{J_c} - N}{2^{J_c}} + \frac{N}{2^{J_c}} \cos(\Delta_c u) \quad (5.8)$$

where $\Delta_c = \Delta\rho_c/\bar{\rho}$. It is very well known that the “standard” measures of skewness and kurtosis, i.e. eqs.(5.1) and (5.2), for the distribution (5.6) can be calculated from the characteristic function (5.8). The results are

$$S = -\frac{1}{i\sigma^3} \left[\frac{d^3\phi_c(u)}{du^3} \right]_{u=0} = 0 \quad (5.9)$$

and

$$K = \frac{1}{\sigma^4} \left[\frac{d^4\phi_c(u)}{du^4} \right]_{u=0} - 3 = \frac{2^{J_c}}{N} - 3, \quad (5.10)$$

where

$$\sigma^2 = -\frac{d^2\phi_c(u)}{du^2} \Big|_{u=0} = \frac{N(\Delta_c)^2}{2^{J_c}} \quad (5.11)$$

is the variance of the distribution.

Consider density fields consisting of clumps or valleys randomly distributed in a background. In this case, the characteristic function is $\phi(u) = \phi_c(u)\phi_b(u)$, where $\phi_b(u)$ is the characteristic function of the background distribution. For a randomly uniform Gaussian background with variance σ_b^2 , the overall variance is

$$\sigma^2 = \frac{N(\Delta_c)^2}{2^{J_c}} + \sigma_b^2, \quad (5.12)$$

and the “standard” kurtosis is

$$K = \left(\frac{2^{J_c}}{N} - 3 \right) \left(1 + \frac{2^{J_c}}{N(s/n)^2} \right)^{-2}, \quad (5.13)$$

where $s/n = \Delta_c/\sigma_b$ is the signal-to-noise ratio. Eq.(5.13) shows that this distribution becomes Gaussian when s/n is small.

Samples of clumps and valleys randomly distributed in Gaussian noise background were produced. Figure 5 shows typical fields which contain A) 16, B) 32, and C) 48 clumps and valleys randomly distributed in white noise background over the range $L = 512$ bins. The signal-to-noise ratio is $s/n = 2.0$, and the size of the clumps, d , is randomly distributed from 1 to 5 bins, i.e. the average bin width of the clumps is about 3. Figure 5 shows the spectrum of kurtosis of these samples. For comparison, the “standard” kurtosis, K , given by eq.(5.2) is also plotted at the position $j = 9$.

When distributions are non-Gaussian, a Gaussian variance will no longer be applicable to estimate the statistical errors. Instead, the error should be calculated from the confidence level of an ensemble of the samples. In Figure 5, the error bars are the 95% confidence for the ensemble consisting of 100 realizations.

Figure 5 shows that the “standard” measure of kurtosis K is generally lower than that given by the FFCs, especially when the number of clumps is large. Moreover, the errors in K are much larger than that of the FFCs, and $K = 0$ is contained in the error bars of K . In other words, K is incapable of detecting the non-Gaussianity of these samples. This is expected because the measure (5.2) is essentially the same as that of the MFCs. As mentioned in §3, the MFC one-point distributions will be Gaussian if the clumps are independent and numerous. On the other hand, the spectrum of kurtosis confirms the non-Gaussianity of the distribution, even when the number of clumps is as large as 48. The spectra also show a peak at $j = 6$ which corresponds to the mean width of the clumps, ~ 3 .

5.3 Suppression of shot noise

LSS data yield distributions sampled with a finite number of objects. Such sampling leads to non-Gaussian signals. Even if the original random field is Gaussian, the sampled data must be non-Gaussian on scales for which the mean number in one bin is small. This is the non-Gaussianity of shot noise. Any non-Gaussian behavior of the density fields will be contaminated by the shot noise.

For instance, in numerical calculations, a distribution $\epsilon(x)$ of sampled objects is often binned into a histogram, and in order to maximally pick up information from a real data set, the bin size is taken to be the resolution of the coordinate x . However when the bin size of the histogram is less than the mean distance of neighbor objects, the value of the binned $\epsilon(x)$ will typically be 0 or 1. Thus, the sample is actually a $d=1$ clump distribution with a one point distribution given by eqs.(5.5) and (5.6). It is *not* a Gaussian distribution. Maximally picking up information about the distribution comes at a cost of artificially introducing non-Gaussian behavior.

It is difficult to separate the non-Gaussianities caused by shot noise and binning with that given by non-Gaussian structures. The measure K contains all contributions to the non-Gaussianity of the density field. As a consequence, K will be sampling-dependent, and not suitable for confronting

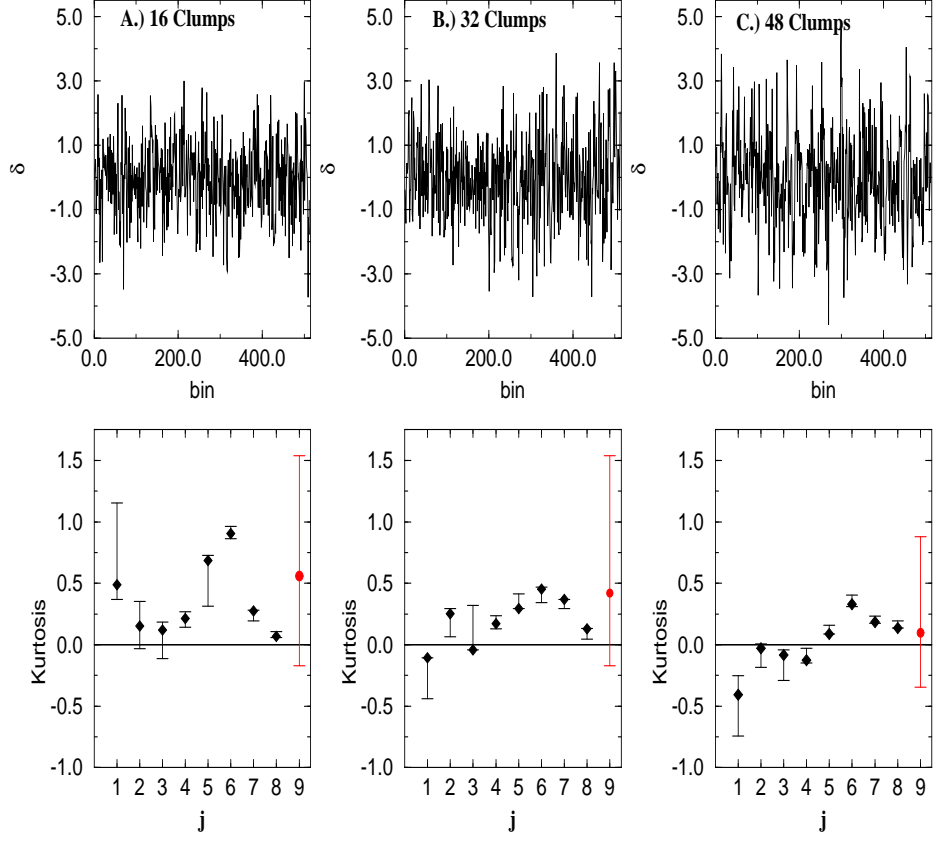


Figure 5: Kurtosis spectra for samples consisting of 16, 32, and 48 clumps in a length of $L = 512$ bins. The sizes of the clumps, d , are randomly distributed in range of 1 to 5 bins. S/N is 2.

observation with theory, or for discriminating among models.

However, non-Gaussian shot noise or binning have different spectrum features from that of non-Gaussian samples. For shot noise, the distributions on large scales is a superposition of the small scale field. According to the central limit theorem the non-Gaussian shot noise will rapidly approach zero on larger scales. In other words, if the mean number in a bin is larger for larger bins, the one-point distribution of shot noise will become Gaussian on larger scales. The values of $|K_j|$ for shot noise should rapidly approach zero as j gets smaller, i.e. their kurtosis spectrum should be monotonously decreasing with decreasing j .

To illustrate this point, Figure 6 plots the spectrum of kurtosis for a random white noise sample given by

$$x_i = x_1 + (x_2 - x_1) \cdot RAN \quad (5.14)$$

where x_i is the position of i -th object, and RAN is random number in $(0, 1)$. We take the size of the sample $(x_2 - x_1) = 64$ bins, and the total number of objects is 120. Figure 6 shows that the

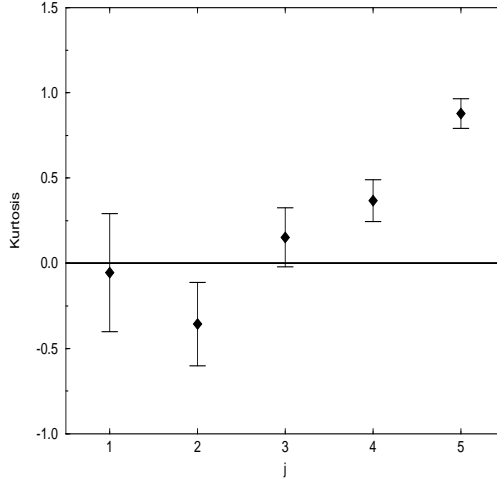


Figure 6: Kurtosis spectrum of 120 objects randomly distributed in 64 bins.

non-Gaussianity of the random sample is significant only when the mean number of objects per bin is less than 2.

The non-Gaussianity of the shot noise will significantly be suppressed in the spectrum of FFC cumulants with increasing scale. This feature is useful in distinguishing between non-Gaussian clumps and shot noise. For instance, one can definitely conclude the existence of non-Gaussian structures if the kurtosis spectrum is flat, or contains peaks as in Figure 5.

6 A preliminary result using DWT: $\text{Ly}\alpha$ forests

6.1 LSS Problems of $\text{Ly}\alpha$ clouds

$\text{Ly}\alpha$ absorption line forests in QSO spectra come from intervening absorbers, or clouds, with neutral hydrogen column densities ranging from about 10^{13} to 10^{17} cm^{-2} at high redshifts. Since the size of the $\text{Ly}\alpha$ clouds at high redshift is as large as $100 - 200 h^{-1} \text{ Kpc}$, and their velocity dispersion is as low as $\sim 100 \text{ km s}^{-1}$ (Bechtold et al. 1994, Dinshaw et al. 1995, Fang et al. 1996), it is generally believed that the $\text{Ly}\alpha$ clouds are probably neither virialized nor completely gravity-confined, but given by pre-collapsed areas in the density field. It is reasonable to assume that the $\text{Ly}\alpha$ clouds joined the clustering process in the universe.

However, almost all of the results drawn from two-point correlation function analysis of $\text{Ly}\alpha$ forest lines have failed to detect any significant clustering on the scales less than $10 h^{-1} \text{ Mpc}$ (Weymann 1993), where h is the Hubble constant in the unit of $100 \text{ km s}^{-1} \text{ Mpc}^{-1}$. In other words, the power spectrum of the $\text{Ly}\alpha$ clouds is flat, i.e. similar to white noise.

Theoretically, it is hard to believe that the distribution of the Ly α lines is only white noise since the Ly α clouds should be formed via the same process as that for other objects, i.e., gravitational clustering. In fact, contrary to the results of two point correlation function, statistics based on other methods show definite deviations of the Ly α forests from a uniform random distribution. For instance, the distribution of nearest neighbor Ly α line intervals was found to be significantly different from a Poisson distribution (Liu and Jones 1990). Based on the Kolmogorov-Smirnoff (K-S) statistic, Ly α absorbers have been shown to deviate from a uniform distribution at $\sim 3\sigma$ significant level (Fang, 1991).

It is of fundamental importance to understand why the two point correlation function, which is one of the most used ways to detect structure, fails to detect any clustering when other methods are showing definite structure. Two possible explanations are 1.) the clustering cannot be detected by the two-point correlation function on scale less than $10 h^{-1}$ Mpc, 2.) the clustering cannot be detected by second order statistics. We look at these in more detail.

1. If the spectrum of Ly α clouds is different from white noise only on large scales, the clustering will be missed by the two point correlation function. As we know, the mean number density of the Ly α clouds significantly evolves with redshift. The evolution is generally described as

$$\frac{dN}{dz} = \left(\frac{dN}{dz} \right)_0 (1+z)^\gamma \quad (6.1)$$

where $(dN/dz)_0$ is the number density extrapolated to zero redshift, and $\gamma \sim 2$ the index of evolution. No mean density is available for calculating the two-point correlation function. Since the correlation amplitudes are less than the uncertainty of mean density of Ly α lines on scales larger than $5 h^{-1}$ Mpc, the two-point correlation will overlook structures on large scales.

2. If the clustering of Ly α clouds cannot be detected by second order statistics, the two-point correlation function will certainly be incapable of detecting structures. Using a linear simulation of density fields, it is found that the simulated clouds indeed show no power of their two-point correlation functions on scales from about 100 km s^{-1} to 2000 km s^{-1} (see Figure 7) (Bi, Ge & Fang 1995, hereafter BGF). Since the perturbation spectrum used for the simulation is not white noise, the distribution of the clouds should contain large scale structures. No power in the line-line correlations may not mean that the distribution is white noise, but instead indicate, that the two-point correlation function sometimes is ineffective in detecting structures on large scales.

In order to clarify clustering of the Ly α clouds we need to determine whether: A.) does the power spectrum of Ly α clouds stay flat on large scales? B.) is the clustering of the clouds detectable by higher order statistics?

6.2 Flatness of power spectrum

Question A can be answered by a DWT spectrum detection. We will look at two popular real data sets of the Ly α forests. The first was compiled by Lu, Wolfe and Turnshek (1991, hereafter LWT). The total sample contains ~ 950 lines from the spectra of 38 QSO that exhibit neither broad

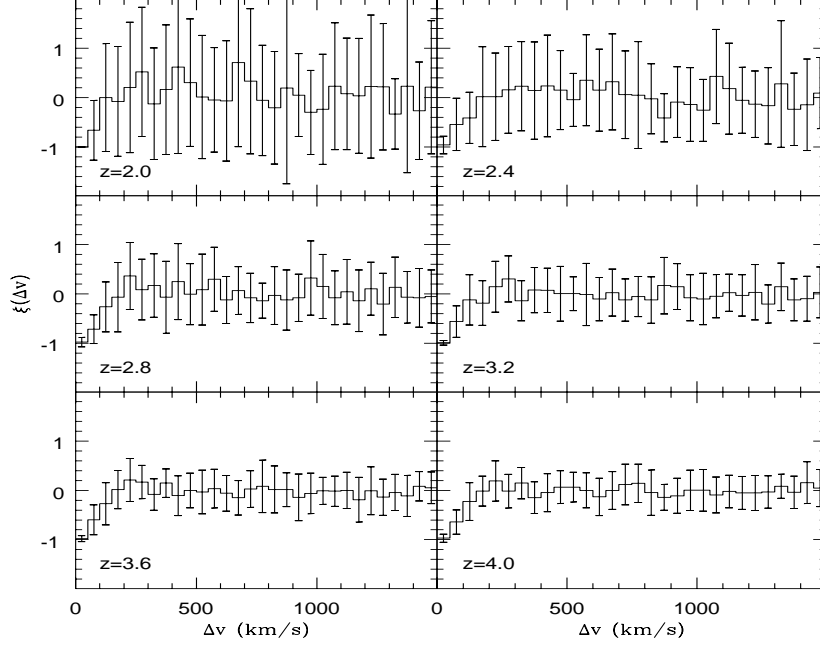


Figure 7: Two-point correlation functions of the BGF simulated sample of $\text{Ly}\alpha$ forests with $W \geq 0.16\text{\AA}$ in the LCDM . The error bars represent 1σ .

absorption lines nor metal line systems. The second set is from Bechtold (1994, hereafter JB), which contains a total ~ 2800 lines from 78 QSO's spectra, in which 34 high redshift QSOs were observed at moderate resolution. To eliminate the proximity effect, all lines with $z \geq z_{em} - 0.15$ were deleted from our samples. These samples cover a redshift range of 1.7 to 4.1, and a comoving distance range from about $D_{min}=2,300 h^{-1}\text{Mpc}$ to $D_{max}=3,300 h^{-1}\text{Mpc}$, if $q_0 = 1/2$.

For comparison, we also work on the simulation samples of BGF. The density fields in this simulation are generated as Gaussian perturbations with a linear power spectrum given by the standard cold dark matter model (SCDM), the cold plus hot dark matter model (CHDM), and the low-density flat cold dark matter model (LCDM). The baryonic matter is assumed to trace the dark matter distribution on scales larger than the Jeans length of the baryonic gas, but is smooth over structures on scales less than the Jeans length. Within a reasonable range of the UV background radiation at high redshift, the absorption of the pre-collapsed baryonic clouds is found to be in good agreement with the features of $\text{Ly}\alpha$ forest. In particular, the LCDM gives good fits to: 1) the number density of $\text{Ly}\alpha$ lines; 2) the distribution of equivalent width; and 3) the redshift-dependence of the line number.

Because different QSO's forest of real samples cover different redshift ranges, it is not trivial to directly find the Fourier power spectrum from an ensemble consisting of such geometrically complex forests. However, this complex geometry can easily be regularized by the method described in §3. Using this technique, all samples were extended in comoving space, to cover 1024 bins with each

bin of comoving size $\sim 2.5 \text{ h}^{-1} \text{ Mpc}$. Thus, all QSO samples were treated uniformly. The Fourier spectrum can then be detected by the FFCs. When we are only interested in the shape, not the amplitude of the spectrum, the result is independent of the uncertainty of overall mean density.

The spectra of LWT($W > 0.36\text{\AA}$), JB($W > 0.32\text{\AA}$) and JB($W > 0.16\text{\AA}$) in the entire redshift range $1.7 < z < 4.1$ are plotted in Figures 8a, b, c, respectively. For comparison, Figure 9 shows the spectra of LWT($W > 0.36\text{\AA}$), JB($W > 0.32\text{\AA}$), SCDM and CHDM with $W > 0.32\text{\AA}$. The error bars in the Figures 8, 9 come from the average over the samples of QSO's absorption spectrum. The errors at large scale are about the same as that on small scales. This means that the spectrum can uniformly be detected on scales as large as about $80 \text{ h}^{-1} \text{ Mpc}$ by the FFCs.

All spectra in Figures 8 and 9 are rather flat on the range of $\log k > -1$, i.e. on scales less than $5 \text{ h}^{-1} \text{ Mpc}$, and slightly increases with scale in a range of $10 - 80 \text{ h}^{-1} \text{ Mpc}$ ($\log k \leq -1$). These results are consistent with the result of no correlation power on scales less than $10 \text{ h}^{-1} \text{ Mpc}$. The flatness of these spectra can be described by the power law index α , which is found by fitting the observed spectra with power law $P(k) \propto k^\alpha$. The results are: $\alpha = -0.26 \pm 0.42$ for the LWT ($W > 0.36\text{\AA}$), $\alpha = -0.23 \pm 0.41$ for the JB ($W > 0.32\text{\AA}$), and $\alpha = -0.23 \pm 0.37$ for the JB ($W > 0.16\text{\AA}$). The two independent data sets, LWT and JB, show almost the same values of the index α . This strongly implies that this feature is common among the Ly α forests.

One can conclude that although the power spectrum seems to increase on large scales, as discussed in §6.1, the values of α and its errors show that the distribution of the real sample is consistent with a flat spectrum ($\alpha \sim 0$) on scales less than $100 \text{ h}^{-1} \text{ Mpc}$. Moreover, the power spectra of the simulated samples of the SCDM, CHDM and LCDM also are quite flat, i.e. $\alpha = -0.93 \pm 0.15$ for SCDM ($W > 0.16\text{\AA}$) and $\alpha = -1.06 \pm 0.08$ for CHDM ($W > 0.16\text{\AA}$). It appears that the difference in the results drawn from the 2-point correlation function and other statistical methods is not due to the possibility that the structures occur on large scales.

6.3 Kurtosis on large scales

From the flatness of the spectrum, it should not be concluded that the distribution of Ly α clouds must be white noise. Instead, this may indicate that the power spectrum and two-point correlation function are not suitable for describing the statistical features of the system being considered. Statistically, it is essential to measure non-Gaussianity in order to detect the clustering of density field with flat power spectrum.

This point can be illustrated by the simulation sample BGF. As shown in Figure 7, the power spectrum of the SCDM ($W > 0.36\text{\AA}$) is flat. The spectrum is almost the same as that of a random sample generated by eq.(5.14) with the redshift-dependence of the number density of the Ly α lines included. That is, in each redshift range $\Delta z = 0.4$ the number of lines in the random sample is taken to be the same as the SCDM sample.

However, Figure 10 shows that the amplitude of the kurtosis spectrum for the SCDM sample is systematically larger than the random sample. Recall that the error bars in Figure 10 do not

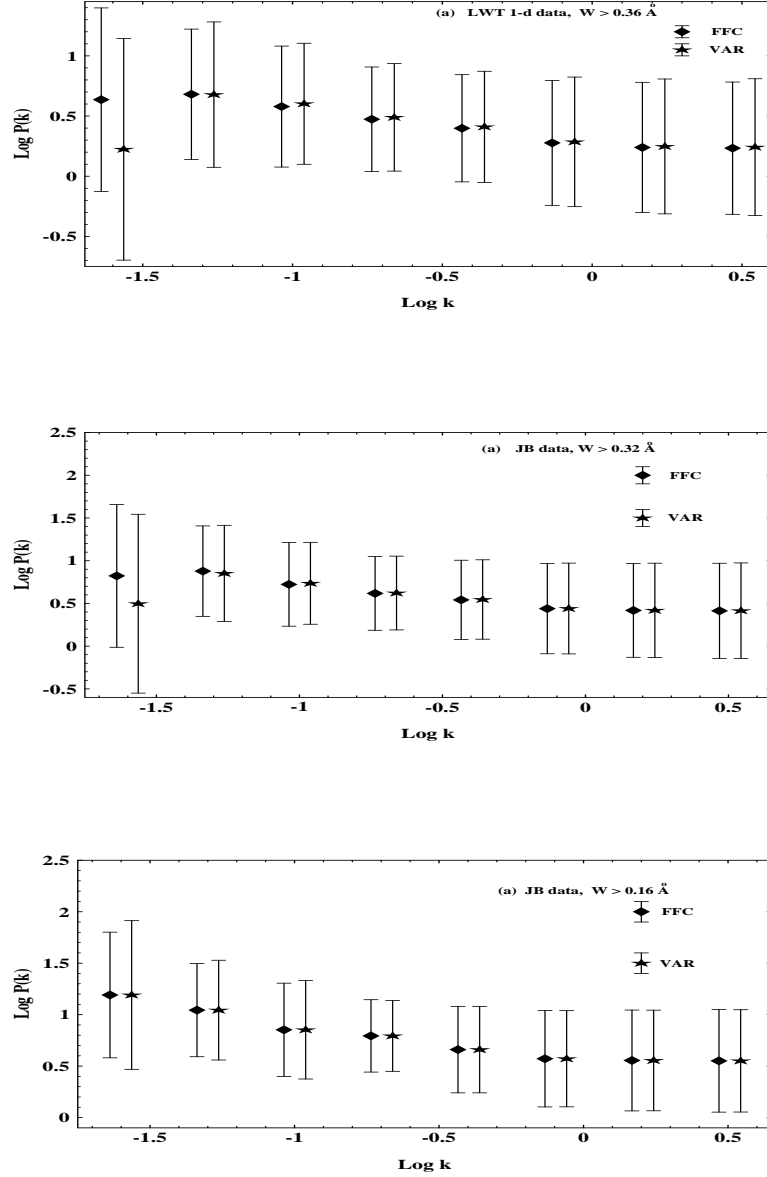


Figure 8: 1-D spectra $P(k)_j$ (diamond) and $P^{var}(k)_j$ (star) of a.) LWT Ly α forest samples with width $> 0.36 \text{ \AA}$; b.) JB with $W > 0.32 \text{ \AA}$ and c.) JB with $W > 0.16 \text{ \AA}$. For clarity, the points $P^{var}(k)_j$ are plotted at $\log k + 0.05$.

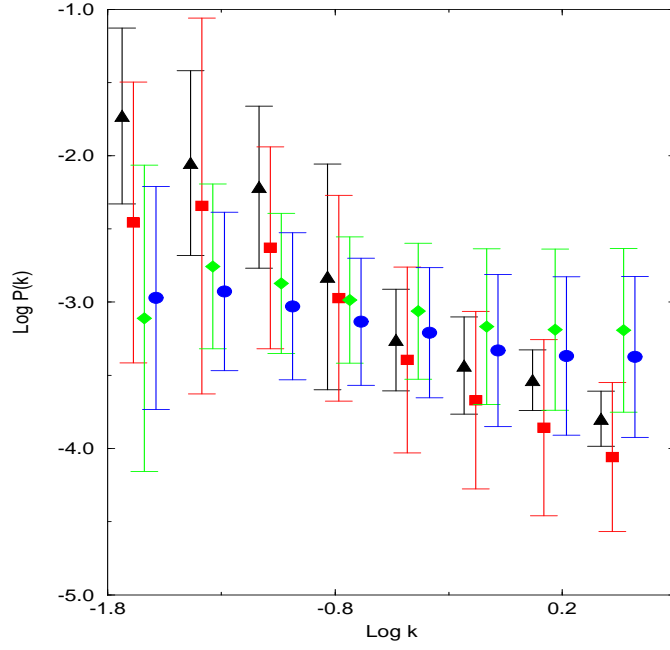


Figure 9: 1-D spectra $P(k)_j$ of LWT Ly α forest samples with width $> 0.36 \text{ \AA}$ (circle); JB samples with $W > 0.32 \text{ \AA}$ (diamond); SCDM with $W > 0.32 \text{ \AA}$ (triangle); CHDM with $W > 0.32 \text{ \AA}$ (square). The spectrum is given by data in the entire redshift range $1.7 < z < 4.1$. k is in unit $h \text{ Mpc}^{-1}$. The error bars are obtained from the average over the samples of QSO's absorption spectrum. For clarity, the four types of points are slightly shifted from each others along the k axis.

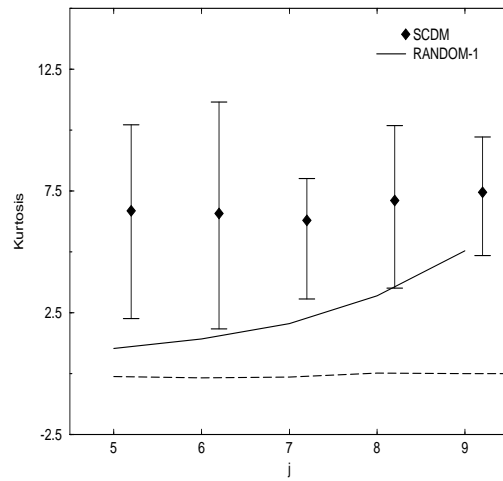


Figure 10: Kurtosis spectra of BGF sample of SCDM model and random data (solid line), respectively. Dot line is for $K_j = 0$.

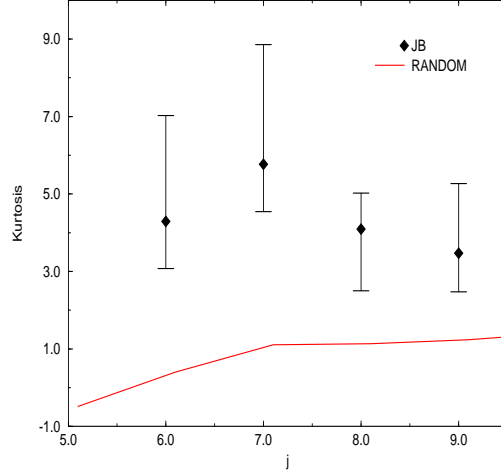


Figure 11: Kurtosis spectra for JB data ($W > 0.16\text{\AA}$), and random sample (dashed line).

represent the 1σ Gaussian errors, but the 95% confidence level from the ensemble of the samples. The difference between the spectra of the SCDM and random sample is significant. The kurtosis of the random sample is completely given by the shot noise. As expected, the kurtosis of the random sample is monotonously decreasing with decreasing of j .

In trying to apply this technique to observational data, one immediately encounters a serious problem. In order to compute the skewness and kurtosis spectrum of real data, subsets of the samples are needed for eqs.(5.3) and (5.4). Unlike the simulated samples, where as much data as needed can be generated, the available real data are limited. There are only $N_r = 43$ samples (forests) for LWT and 78 for JB. In order to effectively use this data, $M \leq N_r$ files from among the complete N_T samples are chosen to form a subset. Various combinations of the subsets M are then combined to form an ensemble. To investigate the effect of different combinations, the subsets M are formed by varying the total number of files chosen from the parent distribution, N_r , as well as changing the order in which the individual files are selected. It is found that the skewness and kurtosis calculated from these M -file ensembles are very stable until M contains as few as 7 or 8 files, i.e. until only approximately 5% of the total lines remain in the subset. The 95 % confidence intervals are then estimated from the ensembles.

Figure 11 shows the kurtosis spectra of the JB data and its random sample. The difference between JB sample ($W > 0.16\text{\AA}$) and random sample is more significant than the difference between SCDM and random data. The amplitudes of the kurtosis spectrum are much higher than that of random data on scales larger than $10\text{ h}^{-1}\text{Mpc}$. Figures 12 and 13 show the skewness and kurtosis spectra of the LWT ($W > 0.36\text{\AA}$) and JB ($W > 0.32\text{\AA}$) data sets. Again, the two independent data sets show the same statistical features. One can conclude that the clustering of the $\text{Ly}\alpha$ clouds can only be clearly described by higher (than 2) order statistics. The distribution of the clouds is non-Gaussian on all scales being detected, i.e. less than $80\text{ h}^{-1}\text{Mpc}$.

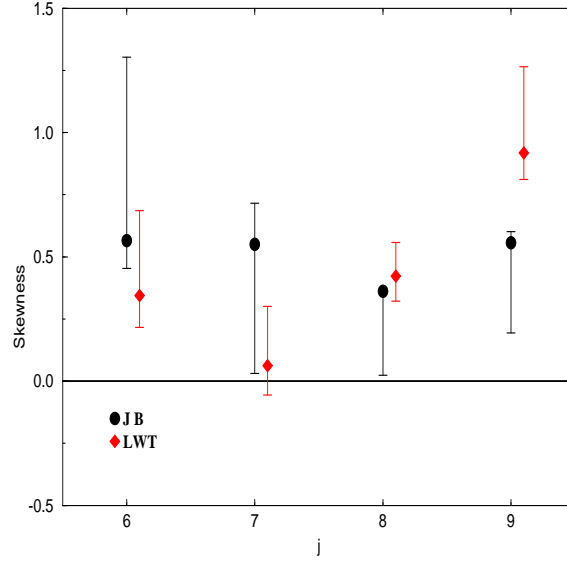


Figure 12: Skewness spectra for samples of LWT ($W > 0.36\text{\AA}$) and JB ($W > 0.32\text{\AA}$).

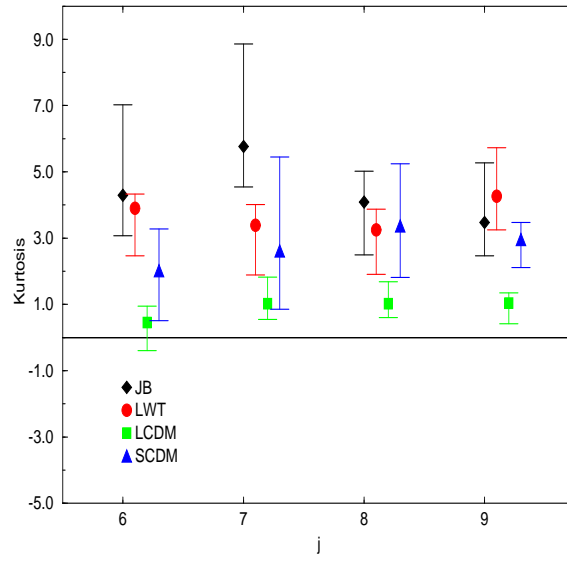


Figure 13: Kurtosis spectra for samples of LWT ($W > 0.36\text{\AA}$) and JB ($W > 0.32\text{\AA}$).

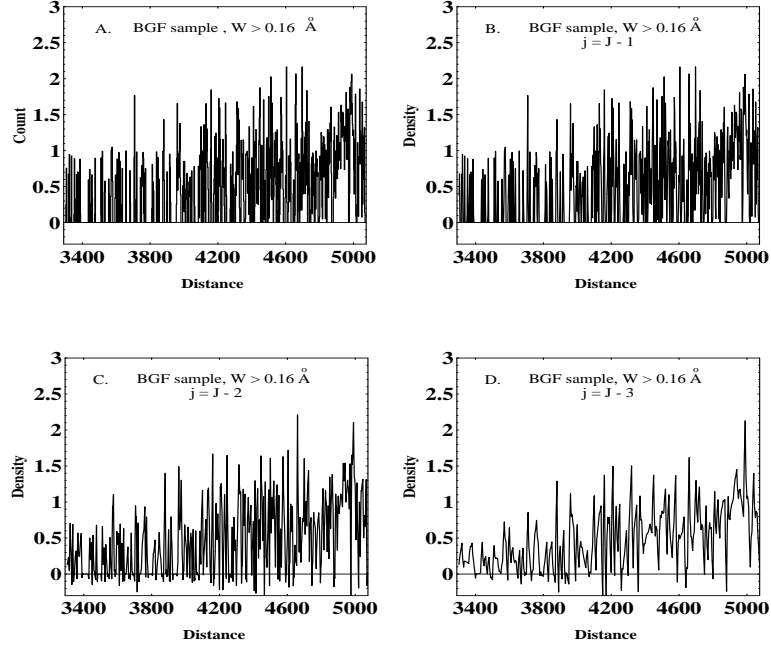


Figure 14: A section of the wavelet reconstruction of density fields for the BGF sample with $W > 0.16\text{Å}$. A. the original (or scale $j = 10$) line distribution. B. C. and D. the reconstructed fields for scale $j = 9, 8$, and 7 , respectively. The distance is in units of $h^{-1}\text{Mpc}$.

6.4 Structures identified by multiresolution analysis

Direct identification of structures is important in the description of LSS, because it allows us to “see” the clustering of object’s distribution and to compare the clusters of simulated samples with observations.

For weakly clustered distributions, it is difficult, even impossible, to distinguish the clusters caused by dynamical interaction with that of random fluctuations. Many clusters are identified at the 2 or 3σ confidence levels. If the identification is done on a large number of realizations, some 3σ events may be due to random processes. We will discuss a method of identifying structures by a DWT multiresolution, in particular, how to handle the random fluctuations in order to get robust conclusions even when the identified clusters are contaminated by random fluctuations.

The DWT multiresolution is based on eqs.(2.20) and (2.48). For a given distribution $\epsilon(x)$, one can decompose it into $\epsilon^j(x)$ on various scales. As an example, Figure 14 shows the original distribution of the LCDM ($W > 0.16\text{Å}$) ($j = 10$), and the result of the reconstruction on $j = 9, 8$ and 7 , corresponding to scales (in comoving space) of about $5, 10$ and $20 h^{-1} \text{Mpc}$, respectively.

The peaks in the field $\epsilon^j(x)$ correspond to high density regions, and are possible clusters on scale j . Various methods of structure identification are designed to pick out such high density regions. Since the MFCs, $\epsilon_{j,l}$, represent the density of the field at position l and on scale j , we

can directly identify possible clusters by picking out the peaks of the MFC distribution. Figure 15 shows a section of the MFC reconstructed distribution for the forest of QSO-0237. The error bars in Figure 15 are $1\text{-}\sigma$ calculated from 100 uniformly random samples which match the number of lines in each redshift interval, $\Delta z = 0.4$, of the parent sample QSO-0237. The peaks of $\epsilon_{j,l}$ distribution are identified as clusters of Ly α clouds on scale j and position (l). The strength or richness of the clusters can be measured by $R = \epsilon_{j,l}/\sigma$.

Using this identification scheme, one can count the number strength distribution of clusters, $N_j(> R)$, which is defined as the total number of the clusters on scale j with strength larger than a given R . For the BGF sample of the LCDM ($W < 0.16\text{\AA}$), the $N_j(> R)$ on scales $j = 9, 8$ and 7 is plotted in Figure 16, in which the error bars are given by the average among the 20 BGF simulated samples. For the JB ($W > 0.16\text{\AA}$), the results of $N_j(> R)$ are shown in Figure 17.

The advantage of using the DWT to identify clusters is the ability to systematically study clusters on all scales and with various strengths. It is easy to estimate the number of clusters which are due to fluctuations, because the mother functions $\phi_{j,l}$ are orthogonal with respect to l and each position l corresponds to an independent realization. For instance, when $j = 9$, the MFCs $\epsilon_{j,l}$ are detected from $2^9 = 1024$ realizations. In this case the number of $R \leq 2$ events for white noise should be about $1024 \times 0.03 \sim 30$. The shape of the function $N_j(> R)$ is more important. In the case of white noise, the number strength function normalized at R_0 , i.e. $N_j(> R)/N_j(> R_0)$, should be $\text{erfc}(R)/\text{erfc}(R_0)$, $\text{erfc}(x)$ being the complementary error function. Again, for white noise, the number-strength distributions on different scales should be satisfied the relation $N_j(> R) \sim 2^n N_{j-n}(> R)$.

From Figures 16 and 17, it is easy to see that for both the BGF and JB data, we have $N_j(> R)/N_j(> 2) > \text{erfc}(R)/\text{erfc}(2)$, and $N_j(> R) > 2^n N_{j-n}(> 2)$ for all $R > 2$. Both samples contain clusters not originating from random fluctuations.

6.5 Discrimination among models

Since the DWT can uniformly calculate statistical quantities on different scale and different orders, it provides a more powerful tool to dissect models. In the last few sections, we have performed this dissection on the BGF samples. As mentioned in §6.1 these samples are linear. Nonetheless using traditional tests, such as the number density, two-point correlation function, the Gunn-Peterson effect etc, they show the same behavior as the observational data. However, these tests involve at most, second order statistics. If the Ly α clouds have undergone non-linear clustering, we should expect that the BGF samples should not compare with the real data when compared using higher order tests. The results of §6.2 and 6.3, do indeed, confirm this. That is, in terms of second order statistics, the BGF data behaves like the real data, but for higher order tests, the BGF shows significant differences from the LWT and JB data sets.

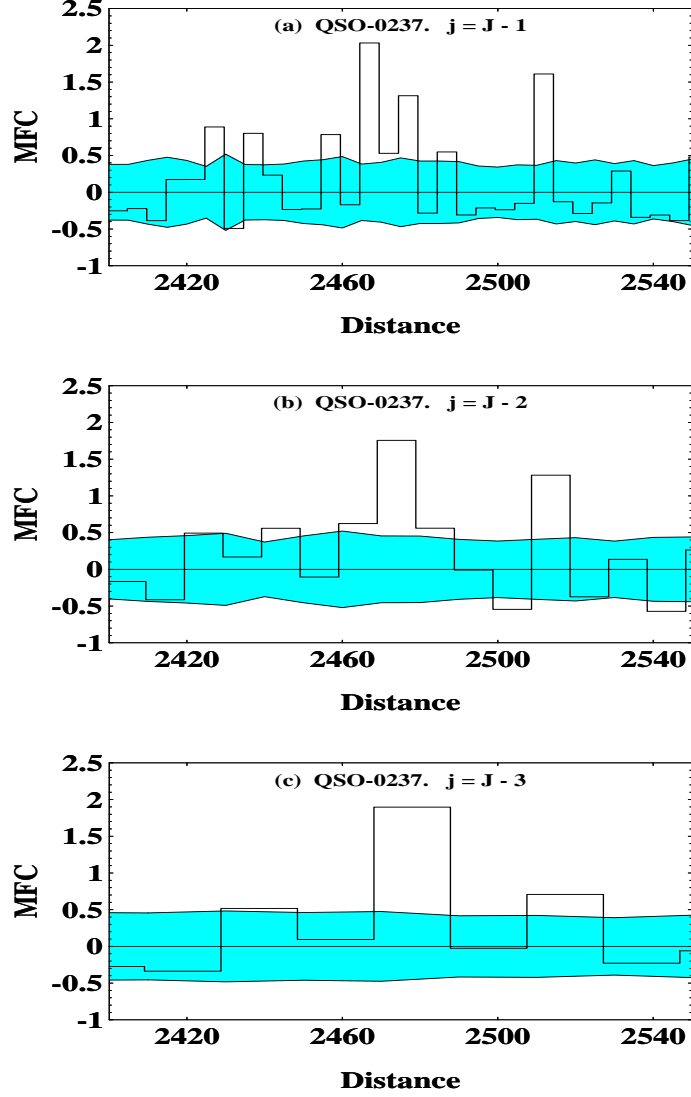


Figure 15: A section of the MFC coefficients of QSO-0237 Ly α forest with line width $W > 0.16 \text{ \AA}$ BGF and the corresponding random samples. A. B. and C. are for scales $j = 9, 8$ and 7 , respectively. The distance is in units of $h^{-1} \text{ Mpc}$. The error bars represent one σ given by 100 random samples. It is interesting to note that the $j = 9$ clusters shown around $2465\text{-}2480 \text{ h}^{-1} \text{ Mpc}$ also appear as $j = 8, 7$ clusters at the same place. That is, this structure appears at all three resolution scales. On the other hand, the structure appearing at $2505\text{-}2520 \text{ Mpc}$ only appears on the scales $j = 9$ and 8 , but not on larger scales.

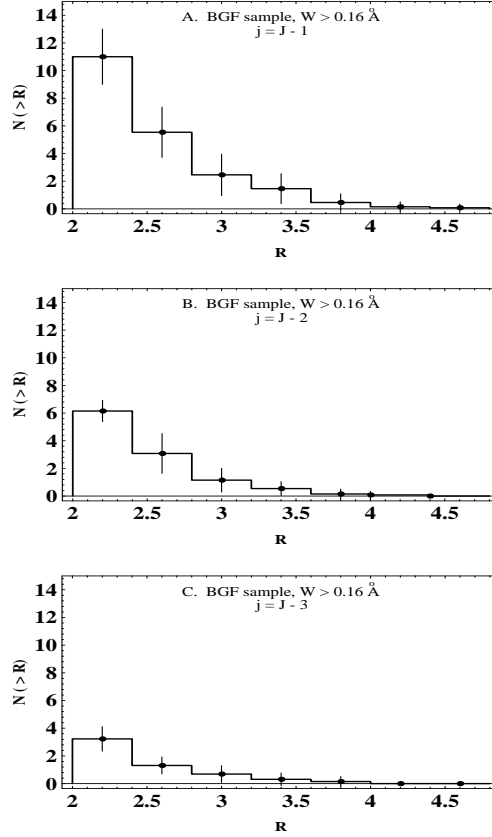


Figure 16: The number of clusters $N_j(> R)$ identified from BGF samples, where R is the richness of the clusters in units of σ . A. B. and C. are for scales $j = 9, 8$ and 7 , respectively. The error comes from average among 20 BGF samples.

For instance, the ratios of $N_j(> R)/N_{j'}(> R)$ and $N_j(> R)/N_j(> R')$ are very dependent on non-Gaussian (i.e. higher order) behavior (§6.3) and so it can also be used as a discriminator. From Figures 16 and 17, one can find that $N_9(> 3.5)/N_9(> 2) = (7 \pm 1.5)\%$ for BGF sample, but $N_9(> 3.5)/N_9(> 2) = 23\%$ and 28% for the LWT and JB data, respectively. The difference of $N_j(> 4)/N_j(> 2)$ between real and simulated sample is more remarkable. Almost no $R > 4.5$ clusters are detected in BGF samples, while they exist in the real sample.

We can recast these results by looking at the redshift-dependence of the number of clusters. As in eq.(6.1), we analyzed the evolution of the number density of clusters on scales $j = 9, 8$, and 7 . The results are plotted in Figure 18. Figure 18a is for LWT ($W > 0.36 \text{ Å}$), and 18b for JB ($W > 0.32 \text{ Å}$). The two data sets showed, once again, the same features. The top curves in Figures 18a and b are the original results (number density of $\text{Ly}\alpha$ lines) of LWT and JB. This number density increases with redshift. However, the number densities of $j = 9, 8$ and 7 clusters show an opposite

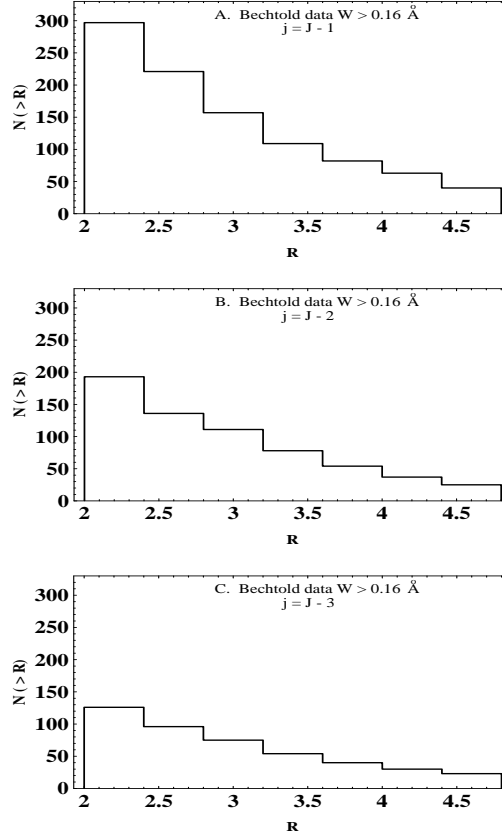


Figure 17: Number of clusters $N_j(> R)$ identified from the JB $W > 0.16\text{\AA}$, where R is the richness of the clusters in units of σ . A. B. and C. are for scales $j = 9, 8$ and 7 , respectively.

evolution, decreasing with increasing redshift. That is, large scale structures traced by $\text{Ly}\alpha$ lines were growing from the era $z = 4$ to 2 . This evolutionary feature was never revealed before the DWT analysis.

We did the same analysis as above with the BGF samples. The results are shown in Figure 19. Figure 19a is for BGF ($W > 0.16\text{\AA}$), and 19b for JB ($W > 0.16\text{\AA}$). We note first that the evolution of the number densities of $j = 9, 8$ and 7 clusters have the same trend as real data: dN/dz is decreasing with redshift. If we fit the curves dN/dz with the power law eq.(16), both the BGF and JB give about the same index γ . This shows that the linear approximation is correct to model the evolutionary trend.

Yet, the values of dN/dz for the $j = 9, 8$ and 7 clusters of the BGF data are less than JB's results by a factor of about 5. Considering that both LWT and JB have about the same number density of $\text{Ly}\alpha$ lines (top curves of Figures 19a and b), the different number density of their clusters should not be fully given by the uncertainty of current observations. The discrepancy is due to the

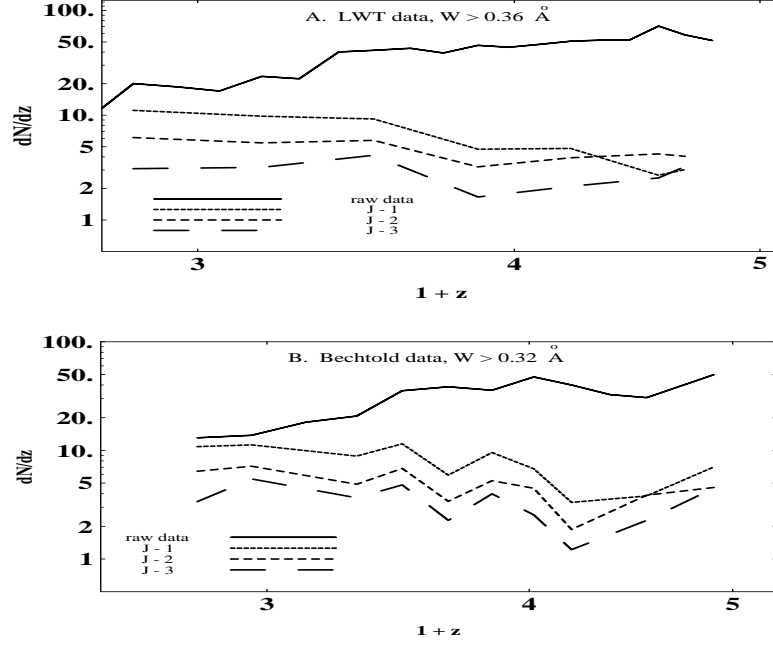


Figure 18: dN/dz vs $(1+z)$ of A. LWT data of $W > 0.36\text{\AA}$, B. JB data of $W > 0.32\text{\AA}$. The top curves are given by original Ly α lines. The lower curves are from the identified clusters on scales $j = 9, 8$ and 7 , respectively.

fact that the linear simulation underestimated clustering on large scales.

7 Miscellaneous topics

Topics included in this section should not be considered less important, but rather, less developed.

1. Scale-dependence of bias

Bias is introduced to describe how the spatial distribution of objects like galaxies and galaxy clusters is related to that of the underlying mass. Theoretically, linear bias b for a given type of object is defined as

$$\epsilon(x)_{object} = b\epsilon(x)_{mass}. \quad (7.1)$$

Applying the DWT eq.(7.1) gives

$$(\epsilon_{j,l})_{objects} = b(\epsilon_{j,l})_{mass}. \quad (7.2)$$

Considering the density field is homogeneous, both $(\epsilon_{j,l})_{objects}$ and $(\epsilon_{j,l})_{mass}$ should be independent of index l . In eq.(7.2), one can replace $\epsilon_{j,l}$ by its average $\sum_{l=0}^{2^j-1} |\epsilon_{j,l}|/2^j$. Generally, $(\epsilon_{j,l})_{objects}$ and $(\epsilon_{j,l})_{mass}$ are j -dependent, and therefore their ratio is also scale-dependent. This is true even for a

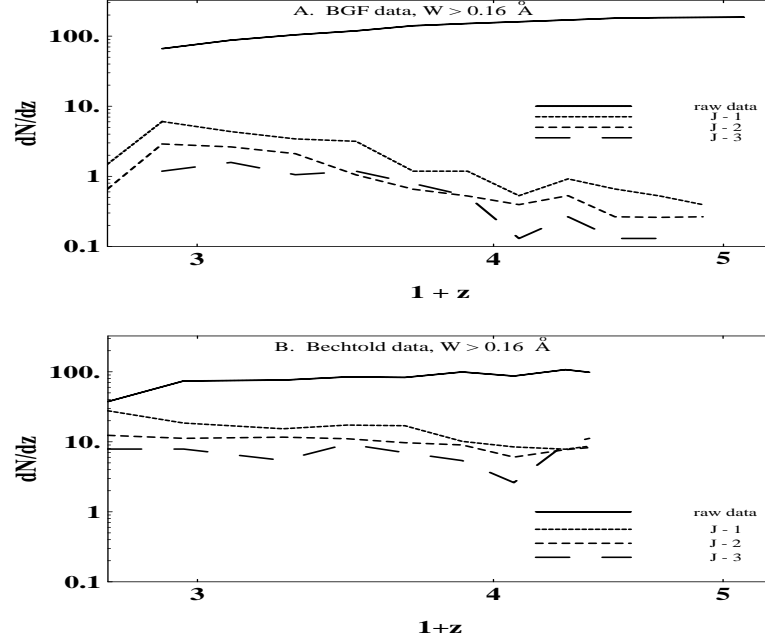


Figure 19: dN/dz vs $(1+z)$ of A. the BGF sample of LCDM with $W > 0.16 \text{ \AA}$, B. JB data of $W > 0.16 \text{ \AA}$. Both top curves are given by original Ly α lines. The lower curves are from the identified clusters on scales $j = 9, 8$ and 7 . The amplitudes of the BGF curves of $j = 9, 8$ and 7 are much lower than the corresponding amplitudes of the Bechtold data.

linear bias, i.e., the factor b is generally scale-dependent. As a consequence, it would be better to define the bias factor of the distribution of object I with respect to object II by FFCs as follows

$$b_j = \frac{(\sum_l |\tilde{\epsilon}_{j,l}|)_I}{(\sum_l |\tilde{\epsilon}_{j,l}|)_{II}} \quad (7.3)$$

where the subscripts I and II denote the FFCs for objects I and II, respectively.

For instance, figures 17 and 20 show that $[N_9(> 2)/N_8(> 2)]_{0.32} > [N_9(> 2)/N_8(> 2)]_{0.16}$, but $[N_8(> 2)/N_7(> 2)]_{0.32} < [N_8(> 2)/N_7(> 2)]_{0.16}$, where the subscripts 0.16 and 0.32 denote the clouds of $W > 0.16 \text{ \AA}$ and $W > 0.32 \text{ \AA}$ of JB samples. This result is not consistent with $b_8 = b_7$, and therefore, the bias factors b_j of $W > 0.16 \text{ \AA}$ clouds with respect to $W > 0.32 \text{ \AA}$ are probably j -dependent. Of course, the uncertainty of the current Ly α forest data is still large. The j -dependence of bias is only a very preliminary result. However, it already shows that the features of a bias factor, like scale-dependence, can properly be described by the FFCs.

Bias essentially is one of the environment-dependent effects. On scales equal to or larger than galaxy clusters, the key parameter of the environment should be the local background density. The DWT provides a uniform procedure to measure the local background density on various scales. It can also transform a point-like distribution to MFCs on various scales, and reconstruct the density

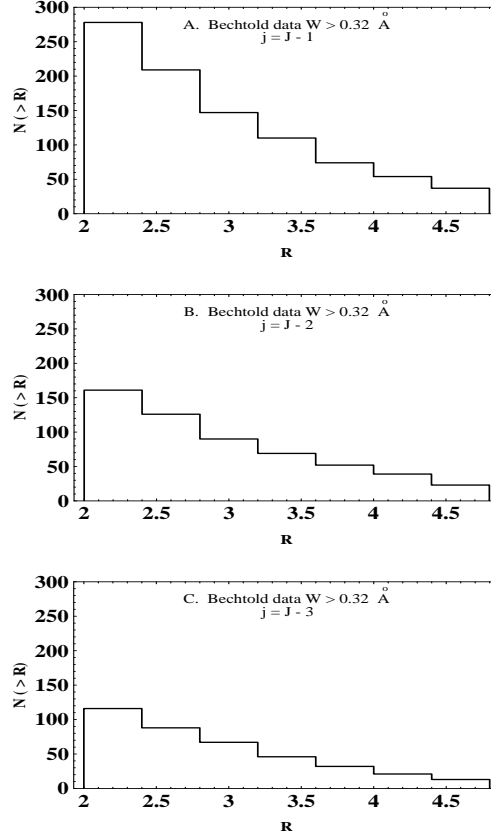


Figure 20: Number of clusters $N_j(> R)$ identified from the JB $W > 0.32 \text{ Å}$, where R is the richness of the clusters in units of σ . A. B. and C. are for scales $j = 9, 8$ and 7 , respectively.

field on various scales. Environmental effects can be revealed by the correlation with MFCs. The cross-correlation between MFC and FFC is particularly important, since it describes how clustering depends on environment.

2. Extraction of fractal

Observational data indicates that the clustering of galaxies seems to be scale-free. On the other hand, a pure fractal distribution contradicts with the observed angular correlations on large scales. A complete picture of the LSS may need to incorporate fractal structures into a homogeneous background (Luo and Schramm 1994). However, on which scale will the fractal features end, and turn to a homogeneous distribution? This issue is a subject in debate. Statistically, we need a method of extracting fractal structures from a homogeneous random background, and detecting the scale of the fractal ending. Since the bases for the DWT are self similar, the choice of the DWT for fractal analysis is a natural one.

To illustrate this point, we consider a Gaussian field with small self-similar (multifractal) structures added. In a conventional multifractal analysis a distribution is first expressed as, for example, eq.(2.10). The scaling behavior is detected by

$$\sum_l |\epsilon_{j,l}|^q \sim 2^{j\tau(q)}. \quad (7.4)$$

For a Gaussian background, $\tau_{Gaussian}(q) = q - 1$. Since the amplitudes $\epsilon_{j,l}$ reflect absolute values, this scaling approach is quite insensitive to the small self-similar component when the large Gaussian background dominates. On the other hand, the FFCs $\tilde{\epsilon}_{j,l}$ focus on differences between neighboring parts of the distribution, and therefore, the smooth Gaussian background drops out for small scales l and the FFCs are only determined by the self-similar component. Hence, the fractal is easily extracted by

$$\sum_l |\tilde{\epsilon}_{j,l}|^q \sim 2^{-j\beta(q)}. \quad (7.5)$$

The fractal component can be detected if $\beta(q)$ is different from $(2q - 1)$. For large j Gaussian behavior take over again. One may then be able to find the scale at which the distribution transforms from a fractal to a Gaussian distribution.

3. Hierarchical clustering and scale-scale correlations

Besides statistical descriptions, the DWT representation could be valuable for dynamical study. Dynamics is certainly representation-independent. Dynamical solutions found in Fourier representation can be found by a DWT mode expansion. Practically, however, different representation are not equivalent because we cannot calculate the mode-mode coupling (or correlations) on all orders, but only on a few lower orders. These lower orders are different for different mode decompositions. In other words, different bases will reveal different aspects of the LSS dynamics. Different selection of the bases functions is necessary to study different aspects of the LSS. To illustrate this point, let's study so-called merging process in structure formation.

In the standard scenario of structure formation, larger dark matter halos are generally considered to form hierarchically from the clustering of smaller halos. One can trace the histories of dark matter halos on the assumption that there is a relation between the halos on different scales. In order to exploit the DWT's ability to extract information of the merging process, several toy models of textures have been investigated. These include the p-model, p-model with random branching, α -model, QCD-motivated cascade model, etc. For instance, similar to the Block model of merge trees (Cole, 1991), the p-model assumes that mass M in a L -th order (scale) object is split unequally into two $L/2$ -th objects. The process repeats, cascading down through scales of length $L/4$, $L/8$,... till the scale L/n . The final distribution generated by p-model is a number density field of L/n -th objects. The two-point correlation function of the L/n -th objects shows the same power-law behavior as usually found in galaxy and other LSS samples.

However, the two-point correlation based on monoscale expansion does not take the hierarchical process into account. In fact, the power-law behavior of the two-point correlation can be realized

in many models. It is not an optimal choice to detect the merging trees. A better choice is the correlation between FFCs on different scales. One can show that for the p-model, the scale-scale correlations of FFCs is completely compressed into the diagonal (Greiner, Lipa, & Carruthers 1995). That is, the scale-scale correlation between FFCs can provide information on how larger structures with substructures living inside are formed. In this sense, the higher order FFC correlation are sensitive to the merging dynamics of the LSS.

8 Outlook

The wavelet transform is a very new technique in physics. As with many other mathematical methods being introduced into physics, the problem in the first phase of development is a lack of feeling for the physical meaning of the relevant mathematical quantities. In the mind of physicists, the Fourier coefficient is not only a result of a mathematical transform, but directly “seen” as an excited mode, a “particle” with a given momentum, the energy of the model etc. On the other hand, the MFCs and FFCs are far from becoming accustomed notions.

This being the case, we should first try to search for a better understanding of the physical meaning of the wavelet coefficients. Fortunately, the wavelet community in different fields of physics has shared much with each other. The DWT is being rapidly introduced in physics including turbulence (Farge 1992), multiparticle dynamics (Greiner et al. 1996, Huang et al. 1996), disordered solid state systems (Kantelhardt, Greiner & Roman 1995) and quantum algebras (Ludu & Greiner 1995). In the context of LSS, the wavelet transform certainly opens new possibilities. The results reviewed here already demonstrate some of the superior properties of the wavelet transform in revealing the physics of LSS. As we become more familiar with the technique and start to build intuition about the MFCs and FFCs, the wavelet transform should reveal yet more information about LSS.

Appendix

A Relationship between Fourier coefficients and FFCs

From eq.(2.41), we have

$$\begin{aligned}
 \tilde{\epsilon}_{j,l+K} &= \int_{-\infty}^{\infty} \epsilon(x) \psi_{j,l+K}(x) dx \\
 &= \int_{-\infty}^{\infty} \epsilon(x) \left(\frac{2^j}{L} \right)^{1/2} \psi(2^j x/L - l - K) dx \\
 &= \int_{-\infty}^{\infty} \epsilon(x' + 2^{-j}KL) \left(\frac{2^j}{L} \right)^{1/2} \psi(2^j x'/L - l) dx' \tag{A1}
 \end{aligned}$$

here we make a change of variable $x' = x - 2^{-j}KL$. Therefore, when $2^{-j}K$ is an integer, i.e. $K = 2^j m$, eq.(A1) is

$$\tilde{\epsilon}_{j,l+2^j m} = \int_{-\infty}^{\infty} \epsilon(x' + mL) \left(\frac{2^j}{L} \right)^{1/2} \psi(2^j x'/L - l) dx' = \tilde{\epsilon}_{j,l} \tag{A2}$$

which shows that the FFC, $\tilde{\epsilon}_{j,l}$, are periodic in l with period 2^j .

Substituting the wavelet expansion of $\epsilon(x)$, i.e. eq.(2.49) into eq.(2.51), we have

$$\epsilon_n = \frac{1}{L} \int_0^L \left[\sum_{j=0}^{\infty} \sum_{l=-\infty}^{\infty} \tilde{\epsilon}_{j,l} \psi_{j,l}(x) \right] e^{-i2\pi n x/L} dx \tag{A3}$$

Using eq.(A2), eq.(A3) becomes

$$\begin{aligned}
 \epsilon_n &= \frac{1}{L} \int_0^L \left[\sum_{j=0}^{\infty} \sum_{l=0}^{2^j-1} \sum_{m=-\infty}^{\infty} \tilde{\epsilon}_{j,l} \psi_{j,l+2^j m}(x) \right] e^{-i2\pi n x/L} dx \\
 &= \frac{1}{L} \sum_{j=0}^{\infty} \sum_{l=0}^{2^j-1} \tilde{\epsilon}_{j,l} \sum_{m=-\infty}^{\infty} \int_0^L \left(\frac{2^j}{L} \right)^{1/2} \psi(2^j x/L - l - 2^j m) e^{-i2\pi n x/L} dx \\
 &= \frac{1}{L} \sum_{j=0}^{\infty} \sum_{l=0}^{2^j-1} \tilde{\epsilon}_{j,l} \int_{-\infty}^{\infty} \left(\frac{2^j}{L} \right)^{1/2} \psi(2^j x'/L - l) e^{-i2\pi n x'/L} dx' \\
 &= \frac{1}{L} \sum_{j=0}^{\infty} \sum_{l=0}^{2^j-1} \tilde{\epsilon}_{j,l} \int_{-\infty}^{\infty} \psi_{j,l}(x') e^{-i2\pi n x'/L} dx' \\
 &= \frac{1}{L} \sum_{j=0}^{\infty} \sum_{l=0}^{2^j-1} \tilde{\epsilon}_{j,l} \hat{\psi}_{j,l}(n) \tag{A4}
 \end{aligned}$$

This is eq.(2.58). An alternative form, which uses the Fourier transform of the basic function $\psi(x)$ rather than $\psi_{j,l}(x)$, can be derived from eq.(A4) as follows

$$\begin{aligned}
\epsilon_n &= \frac{1}{L} \sum_{j=0}^{\infty} \sum_{l=0}^{2^j-1} \tilde{\epsilon}_{j,l} \int_{-\infty}^{\infty} \psi_{j,l}(x) e^{-i2\pi nx/L} dx \\
&= \frac{1}{L} \sum_{j=0}^{\infty} \sum_{l=0}^{2^j-1} \tilde{\epsilon}_{j,l} \int_{-\infty}^{\infty} \left(\frac{2^j}{L}\right)^{1/2} \psi(2^j x/L - l) e^{-i2\pi nx/L} dx \\
&= \frac{1}{L} \sum_{j=0}^{\infty} \sum_{l=0}^{2^j-1} \left(\frac{2^j}{L}\right)^{-1/2} \tilde{\epsilon}_{j,l} e^{-i2\pi nl/2^j} \int_{-\infty}^{\infty} \psi(\eta) e^{-i2\pi n\eta/2^j} d\eta \\
&= \sum_{j=0}^{\infty} \sum_{l=0}^{2^j-1} \left(\frac{1}{2^j L}\right)^{1/2} \tilde{\epsilon}_{j,l} e^{-i2\pi nl/2^j} \hat{\psi}(n/2^j)
\end{aligned} \tag{A5}$$

This is eq.(2.59).

B Parseval theorem of the DWT

From the expansion (2.49) we have

$$\int_0^L |\epsilon(x)|^2 dx = \sum_{j,j'=0}^{\infty} \sum_{l,l'=-\infty}^{\infty} \tilde{\epsilon}_{j,l} \tilde{\epsilon}_{j',l'} \int_0^L \psi_{j,l}(x) \psi_{j',l'}(x) dx \tag{B1}$$

Considering the periodicity (A2), eq.(B1) can be rewritten as

$$\begin{aligned}
&\int_0^L |\epsilon(x)|^2 dx \\
&= \sum_{j,j'=0}^{\infty} \sum_{l=0}^{2^j-1} \sum_{m=-\infty}^{\infty} \sum_{l'=0}^{2^{j'}-1} \sum_{m'=-\infty}^{\infty} \tilde{\epsilon}_{j,l} \tilde{\epsilon}_{j',l'} \int_0^L \psi_{j,l+2^j m}(x) \psi_{j',l'+2^{j'} m'}(x) dx \\
&= \sum_{j,j'=0}^{\infty} \sum_{l=0}^{2^j-1} \sum_{l'=0}^{2^{j'}-1} \tilde{\epsilon}_{j,l} \tilde{\epsilon}_{j',l'} \times \\
&\quad \sum_{m=-\infty}^{\infty} \sum_{m'=-\infty}^{\infty} \frac{2^j}{L} \int_0^L \psi(2^j x/L - l - 2^j m) \psi(2^{j'} x/L - l' - 2^{j'} m') dx \\
&= \sum_{j,j'=0}^{\infty} \sum_{l=0}^{2^j-1} \sum_{l'=0}^{2^{j'}-1} \tilde{\epsilon}_{j,l} \tilde{\epsilon}_{j',l'} \sum_{m'' \equiv (m-m')=-\infty}^{\infty} \sum_{m'=-\infty}^{\infty} \\
&\quad \frac{2^j}{L} \int_0^L \psi(2^j x/L - l - 2^j(m'' + m')) \psi(2^{j'} x/L - l' - 2^{j'} m') dx \\
&= \sum_{j,j'=0}^{\infty} \sum_{l=0}^{2^j-1} \sum_{l'=0}^{2^{j'}-1} \tilde{\epsilon}_{j,l} \tilde{\epsilon}_{j',l'} \times
\end{aligned}$$

$$\begin{aligned}
& \sum_{m''=-\infty}^{\infty} \sum_{m'=-\infty}^{\infty} \frac{2^j}{L} \int_0^L \psi(2^j(x/L - m') - l - 2^j m'') \psi(2^{j'}(x/L - m') - l') dx \\
&= \sum_{j,j'=0}^{\infty} \sum_{l=0}^{2^j-1} \sum_{l'=0}^{2^{j'}-1} \tilde{\epsilon}_{j,l} \tilde{\epsilon}_{j',l'} \times \\
& \quad \sum_{m''=-\infty}^{\infty} \frac{2^j}{L} \int_{-\infty}^{\infty} \psi(2^j x/L - l - 2^j m'') \psi(2^{j'} x/L - l') dx \\
&= \sum_{j,j'=0}^{\infty} \sum_{l=0}^{2^j-1} \sum_{l'=0}^{2^{j'}-1} \tilde{\epsilon}_{j,l} \tilde{\epsilon}_{j',l'} \sum_{m''=-\infty}^{\infty} \int_{-\infty}^{\infty} \psi_{j,l+2^j m''}(x) \psi_{j',l'}(x) dx \\
&= \sum_{j,j'=0}^{\infty} \sum_{l=0}^{2^j-1} \sum_{l'=0}^{2^{j'}-1} \tilde{\epsilon}_{j,l} \tilde{\epsilon}_{j',l'} \sum_{m''=-\infty}^{\infty} \delta_{j,j'} \delta_{l+2^j m'',l'} \tag{B2}
\end{aligned}$$

From $\delta_{j,j'}$, j' should be equal to j , and then $l' < 2^j$. Therefore, $\delta_{l+2^j m'',l'}$ requires $m'' = 0$ and $l = l'$. We have then the Parseval theorem (4.3).

C References

- Adler, R.J. 1981, *The Geometry of Random Field*, (New York, Wiley) Barbero, J.F., Dominguez, A., Goldman, T. & Pérez-mercader, J. 1996, Los Alamos preprint LAEFF-96/15 Berera, A. & Fang, L.Z. 1994, Phys. Rev. Lett, 72, 458 Bechtold, J. 1994, Astrophys. J. Supp. 91, 1 (JB) Bechtold, J., Crots, P.S., Duncan, R.C. & Fang Y. 1994, Astrophys. J. 437, L83 Bi, H.G., Ge, J. & Fang, L.Z. 1995, Astrophys. J. 452, 90, (BGF) Carruthers, P. 1995, XXIII International Symposium on Multiparticle Dynamics, Aspen Colorado, World Scientific, Singapore, to be published. Chui, C.K. 1992, *Wavelets: A Tutorial in Theory and Applications*, Academic Press Cole, S. 1991, ApJ. 367, 45. Daubechies, I. 1988, Comm. Pure. Appl. Math. 41, 909. Daubechies, I. 1992, *Ten Lectures on Wavelets*, (SIAM) Finkelshaw, N., Foltz, C.B., Impey, Weymann, R. & Morris, S.L. 1995, Nature, 373, 223 Gfstathiou, G., Kaiser, N., Saunders, W., Lawrence, A., Rowan-Robinson, M., Ellis, R.S. & Frenk, C.S. 1990, Mon. Not. R. Astr. Soc. 247, 10p Scalera, E. & Mazure, A. 1992, Astrophys. J. 388, 23 Scalera, E., Slezak, E. & Mazure, A. 1992, Ast. & Astrophys. 264, 379 Fan, Z.H. & Bardeen, J.M. 1995, Phys. Rev. D51, 6714 Fang, L.Z. 1991, Astr. & Astrophys. 244, 1. Fang, Y.H., Duncan, R.C., Crots, A.P.S. & Bechtold, J., Astrophys. J., 462, 77 Farge, M. 1992, Ann. Rev. Fluid Mech., 24, 395 Feiner, M., Lipa, P. & Carruthers, P. 1995, Phys. Rev. E51, 1948 Feiner, M., Giesemann, J., Lipa, P. & Carruthers, P. 1996, Z. Phys. C.69, 305 Huang, Z. Sarcevic, I., Thews, R. & Wang, X.N. 1996, Phys. Rev. D. 54, 750 Ivanov, A.V. & Leonenko, N.N. 1989, *Statistical analysis of Random Field*, Klumer Academic Pub. Kaiser, G. 1994, Applied & Computational Harmonic Analysis, 1, 246. Kaiser, N. & Peacock, J.A. 1991, Astrophys. J. 379, 482 Kantelhardt, J., Greiner, M. & Roman, E. 1995, Physica, A220, 219 Kolb, E.W. & Turner, M.S. 1989, *The Early Universe*, Addison-Wesley Pub. Co. Liu, X.D. & Jones, B.J.T. 1990, Mon. Not R. Astr. Soc. 242, 678 Lu, L., Wolfe, A.M., & Turnshek, D.A. 1991, Astrophys. J. 367, 19 (LWT) Udu, A. & Greiner, M. 1995, ICTP-Internal Report IC/95/214 Uo, X. & Schramm, D. 1992, Science, 256, 513 Wallat, S. 1989, Trans. Am. Math. Soc. 315, 69 Wallat, S. & Zhong, S. 1990, Courant Inst. Tech. Rep. No. 483, Martinez, V.J. Paredes, S. & Saar, E. 1993, Mon. Not. R. Astr. Soc. 260, 365 Eyer, Y. 1988, Congr. Int. Phys. Math. July Eyer, Y. 1992, *Wavelets*, (SIAM) Eyer, Y. 1993, *Wavelets: Algorithms and Applications*, SIAM Ando, J. & Fang, L.Z., 1995, astro-ph/9509032 Ando, J. & Fang, L.Z., 1996a, Astrophys. J., 459, 1. Ando, J. & Fang, L.Z., 1996b, astro-ph/9606005 Peebles, P.J.E. 1980, *The Large Scale Structure of the Universe*, Princeton Univ. Press. Perivolaropoulos, L. 1994, Mon. Not. R. Astr. Soc. 267, 529 Press, W.H., Teukolsky, S.A., Vetterling, W.T. & Flannery, B.P. 1992, *Numerical Recipes*, Cambridge Slezak, E., Bijaoui, A. & Mars, G. 1990, Astro & Astrophys, 227, 301 vanmarcke, E, 1983, *Random Field*, MIT Press. Amada, M. & Ohkitani, K. 1991, Prog. Theor. Phys., 86, 799 Eymann, R. J. 1993, in The Environment and Evolution of Galaxies, ed. Shull, J. M. & Thronson, H. A. Jr. 213ickerhauser, M.V. 1994, *Adapted Wavelet Analysis From Theory to Software*, A.K. Peters, Mass